Ridging Associated with Drought across the Western and Southwestern United States: Characteristics, Trends, and Predictability Sources

PETER B. GIBSON AND DUANE E. WALISER

Jet Propulsion Laboratory, California Institute of Technology, Pasadena, California

BIN GUAN

Joint Institute for Regional Earth System Science and Engineering, University of California, Los Angeles, Los Angeles, California

MICHAEL J. DEFLORIO AND F. MARTIN RALPH

Center for Western Weather and Water Extremes, Scripps Institution of Oceanography, University of California, San Diego, La Jolla, California

DANIEL L. SWAIN

Institute of the Environment and Sustainability, University of California, Los Angeles, Los Angeles, California, and Capacity Center for Climate and Weather Extremes, National Center for Atmospheric Research, Boulder, Colorado, and Nature Conservancy of California, San Francisco, California

(Manuscript received 17 June 2019, in final form 12 December 2019)

ABSTRACT

Persistent winter ridging events are a consistent feature of meteorological drought across the western and southwestern United States. In this study, a ridge detection algorithm is developed and applied on daily geopotential height anomalies to track and quantify the diversity of individual ridge characteristics (e.g., position, frequency, magnitude, extent, and persistence). Three dominant ridge types are shown to play important, but differing, roles for influencing the location of landfalling atmospheric rivers (ARs), precipitation, and subsequently meteorological drought. For California, a combination of these ridge types is important for influencing precipitation deficits on daily through seasonal time scales, indicating the various pathways by which ridging can induce drought. Furthermore, both the frequency of ridge types and reduced AR activity are necessary features for explaining drought variability on seasonal time scales across the western and southwestern regions. The three ridge types are found to be associated in different ways with various remote drivers and modes of variability, highlighting possible sources of subseasonal-to-seasonal (S2S) predictability. A comparison between ridge types shows that anomalously large and persistent ridging events relate to different Rossby wave trains across the Pacific with different preferential upstream locations of tropical heating. For the "South-ridge" type, centered over the Southwest, a positive trend is found in both the frequency and persistence of these events across recent decades, likely contributing to observed regional drying. These results illustrate the utility of feature tracking for characterizing a wider range of ridging features that collectively influence precipitation deficits and drought.

1. Introduction

Precipitation across the western and southwestern United States is characterized by large seasonality, variability, and relatively small annual mean totals (Pandey et al. 1999; Dettinger et al. 2011). In California, almost all precipitation falls during the months of October–March, with interannual variability in precipitation (relative to the mean) among the highest across the continental United States (CONUS). In that regard, a relatively small number of storms, often in the form of atmospheric rivers (ARs), can play a key role in determining the outcome of a wet or dry water year (Dettinger 2013). The recent winter of 2015/16 highlighted the

Supplemental information related to this paper is available at the Journals Online website: https://doi.org/10.1175/JCLI-D-19-0439.s1.

Corresponding author: Peter B. Gibson, pgibson@ucsd.edu

DOI: 10.1175/JCLI-D-19-0439.1

immense challenge of seasonal forecasting across these regions. The expectation of drought-breaking precipitation relief, due to the development of one of the largest El Niño events in recent times, was met with the continuation of average or below-average precipitation (Lee et al. 2018; Jong et al. 2018; Chen and Kumar 2018; Singh et al. 2018). While recognizing the immense scientific challenge, improving the reliability of precipitation forecasts beyond ''weather time scales'' and into the subseasonal-to-seasonal (S2S; from 2 weeks to 2 years) range is of great interest and value to water resource managers in this region of intrinsically high hydroclimatic variability (Rayner et al. 2005; Morss et al. 2008; Vitart et al. 2017)

While drought characteristics differ between events, a proximate cause common to meteorological drought in this region is recognized as a broad positive and persistent geopotential height anomaly near or just offshore of the west coast of North America (e.g., Seager and Henderson 2016; Swain et al. 2016, 2017), despite some variability in ridging between drought events (Cook et al. 2018). This anomalous ridging was particularly pronounced across the winters of 2012–16, when severe drought impacted most of the western and southwestern United States. Nicknamed the ''ridiculously resilient ridge'' (Swain 2015) due to its unusual persistence across consecutive winters, this event played an active role in diverting winter storms, including ARs, away from California and surrounding regions (Swain et al. 2014) as was common during historical periods of drought (e.g., Cayan and Roads 1984; Mundhenk et al. 2016; Guirguis et al. 2018).

A grand challenge for improving S2S forecasting relates to better understanding different remote drivers of ridging events and their precursors. Recently, a number of studies have probed links between various modes of variability and the likelihood of ARs making landfall across the western United States (e.g., Guan et al. 2012, 2013; Guan and Waliser 2015; Baggett et al. 2017; Guirguis et al. 2018, 2019; DeFlorio et al. 2018, 2019; Mundhenk et al. 2018; Zhou and Kim 2018). These studies have highlighted potential ''forecasts of opportunity'' for extended AR landfall predictability over S2S time scales, arising from the influence of different modes of variability including El Niño–Southern Oscillation (ENSO), the Pacific–North American teleconnection pattern (PNA), the Madden–Julian oscillation (MJO), and the quasi-biennial oscillation (QBO). A somewhat smaller set of studies, discussed below, have closely examined similar forecasts of opportunity for ridging as they relate to the deficit of ARs and precipitation across the region.

Recent studies focusing on the remote drivers of ridging have given much attention to winters of the 2012–16 drought period that spanned California and parts of the U.S. Southwest. In particular, the relative influence on drought-related ridging from tropical sea surface temperatures (SSTs), sea ice, and internal atmospheric dynamics has been subject to recent debate across this event (e.g., Seager et al. 2015; Seager and Henderson 2016; Teng and Branstator 2017; Swain et al. 2017; Peng et al. 2019; Singh et al. 2018; Chen and Kumar 2018). Seager et al. (2015) and subsequently Seager and Henderson (2016) used model experiments to target optimal patterns of tropical Indo-Pacific SSTs that best reproduced the observed extratropical circulation response. The authors found that the model response was weaker than the observed response but concluded that important drivers include a warm SST anomaly in the western Pacific, a cool anomaly in the central Pacific, and a weak warm anomaly in the Indian Ocean. Teng and Branstator (2017) found that extreme ridges that occurred during winters of 2013/14 and 2014/15 to be part of a continuum of (near-) circumglobal patterns. These circumglobal patterns are trapped in the mean Pacific jet and influenced by the waveguiding effect of the jet. Model simulations suggest that extreme ridges similar to those observed between 2013 and 2015 can be driven by internal midlatitude dynamics alone in the absence of any significant tropical forcing. However, Teng and Branstator (2017) also found that tropical heating anomalies in key regions in the western Pacific, which do not necessarily depend on ENSO, can excite circulation anomalies favorable for extreme ridges, broadly in agreement with Seager and Henderson (2016).

Other recent studies have placed greater emphasis on the importance of tropical and high-latitude forcing. Peng et al. (2019) showed that the influence of tropical forcing was highly variable between months across the winter of 2013/14, and this may be obscured if the seasonal mean is considered in isolation. The authors conclude that MJO-like tropical heating across December 2013 played a large role, after which internal dynamics maintained and amplified this influence across the remainder of the winter season. Swain et al. (2017) derived a relatively simple empirical model from observations to predict ridging as a linear combination of sea ice and SST in different regions, giving focus to the longer historical period (i.e., from 1979 to the present). Although such a model does not explicitly account for random internal dynamical variability, these simple empirical relationships were, to some extent, capable of predicting the winter ridging conditions (based on autumn conditions) during the 2015/16 El Niño event, which were not well predicted by dynamical models (e.g., Jong et al. 2018). While the studies described above reach somewhat differing conclusions regarding the specific relative importance of remote drivers, a common theme is

that some combination of tropical forcing and internal atmospheric variability acting constructively can be important to drought-relevant ridging in these regions. On the other hand, it appears that in certain cases, internal atmospheric variability alone can play a dominant role in driving extreme ridges in any given winter month/season. In cases where tropical forcing is apparent, tropical Rossby wave sources, from regions independent of ENSO, can also play an important role. Further understanding the various processes/phenomena that drive ridging variability and persistence is key to quantifying ridging predictability on S2S time scales, and in turn drought predictability, in the western and southwestern United States.

The studies described above have tended to characterize ridging based on domain-averaged monthly/seasonal height anomalies or correlation with past seasonal analogs. However, even during periods of multiyear drought, drought-related ridging can exhibit considerable variability across time (on submonthly time scales) and across space (i.e., along the West Coast of the United States). As such, useful spatial and temporal information can be lost through monthly/seasonal averaging over a prescribed domain. Evidence in support of this is also provided by Cook et al. (2018), where the authors define different drought types based on typically recurrent spatial patterns of drought. The authors find that different spatial patterns of drought over the western United States relate to distinct patterns of SST with different degrees of tropical forcing versus internal atmospheric dynamics, while similar drought events can be forced by rather different atmospheric ridging patterns (when averaged seasonally). In the present study, we take a different approach by introducing a ridge detection algorithm to track and quantify characteristics of daily geopotential height anomalies associated with precipitation deficits. The output of the ridge detection algorithm is then used to quantify the general characteristics of tracked ridges and how their spatial structure can influence ARs, precipitation, and meteorological drought differently across the western and southwestern regions. We then show that separating out different ridging types, through feature tracking, can provide new insights into trends and possible remote sources of predictability.

2. Data and methods

a. Data

Daily mean geopotential height at 500 hPa from three different reanalysis products were used in this study: MERRA-2 (Gelaro et al. 2017), 20CRV2c (Compo et al. 2011), and ERA-Interim (Dee et al. 2011). These three products were considered to test the sensitivity of results to the particular choice of reanalysis. The use of the extended record 20CRV2c reanalysis (here analyzed for the period 1950–2014) enabled consideration of ridging variability and trends prior to the satellite era, while bearing in mind the additional uncertainty associated with this earlier period. Daily geopotential height anomalies (Z500) were constructed in all reanalyses as departures from the long-term (i.e., across all years) monthly mean in daily fields on a gridcell basis, and used as input to a ridge detection algorithm (see details in section 2b).

MERRA-2 was also used as input to the AR detection algorithm of Guan and Waliser (2015), where 6-hourly integrated water vapor transport (IVT) was computed from specific humidity and wind fields between 1000 and 300 hPa, inclusive. The Guan and Waliser (2015) AR detection algorithm labels atmospheric rivers based upon all of the following conditions being met: IVT exceeding the 85th percentile (seasonal and grid cell-based), IVT exceeding a fixed minimum IVT limit of $100\,\mathrm{kg\,m^{-1}\,s^{-1}}$, length/width ratio greater than 2, and length greater than 2000 km. Other conditions and justification for these thresholds are discussed in detail in Guan and Waliser (2015).

To diagnose different sources of upstream Rossby wave activity that potentially influence ridging across the target region, velocity potential anomalies and wave activity flux (WAF) [Takaya and Nakamura 2001, their Eq. (1.0)] were computed from MERRA-2. The WAF is derived from the conservation of wave-activity pseudomomentum, with WAF vectors parallel to the group velocity of a stationary Rossby wave, thus providing an intuitive view of the pathway of Rossby wave packets through time. Following Takaya and Nakamura (2001) [see Eq. (38) therein] the horizontal wave activity flux W at 250-hPa (here ignoring the vertical) is given by

$$W = \frac{\rho\cos\phi}{2|U|}\begin{pmatrix} \dfrac{U}{a^2\cos^2\phi}\left[\left(\dfrac{\partial\psi'}{\partial\lambda}\right)^2 - \psi'\dfrac{\partial^2\psi'}{\partial\lambda^2}\right] + \dfrac{V}{a^2\cos\phi}\left[\dfrac{\partial\psi'}{\partial\lambda}\dfrac{\partial\psi'}{\partial\phi} - \psi'\dfrac{\partial^2\psi'}{\partial\lambda\,\partial\phi}\right] \\ \dfrac{U}{a^2\cos\phi}\left[\dfrac{\partial\psi'}{\partial\lambda}\dfrac{\partial\psi'}{\partial\phi} - \psi'\dfrac{\partial^2\psi'}{\partial\lambda\,\partial\phi}\right] + \dfrac{V}{a^2}\left[\left(\dfrac{\partial\psi'}{\partial\phi}\right)^2 - \psi'\dfrac{\partial^2\psi'}{\partial\phi^2}\right] \end{pmatrix},$$

where p = (pressure/1000 hPa), a is Earth's radius, ϕ and λ are latitude and longitude, U and V are the time-averaged 250-hPa zonal and meridional winds, and ψ' is the 250-hPa perturbation streamfunction where a 10-day low-pass filter has been applied.

The velocity potential (VP) at 250-hPa was also computed from horizontal wind components. VP is the inverse Laplacian of the divergence, which acts as a strong spatial smoother such that upper-level VP may be used to describe broad regions of large upper-level divergence (Hendon 1986). VP anomalies were computed as departures from the long-term monthly mean in daily fields on a gridcell basis, where a negative (positive) VP anomaly represents broad areas of enhanced (suppressed) convection.

Gridded monthly precipitation data were used to compute state-averaged and basin-averaged precipitation and drought measures. Since precipitation datasets over CONUS can diverge for precipitation estimates over some regions and aspects of precipitation (e.g., Gibson et al. 2019), initial sensitivity testing was performed to compare drought measures between various datasets (Fig. S1 in the online supplemental material). Based on this, the NOAA nClimGrid dataset (Vose et al. 2014) was chosen for subsequent analysis, given its close agreement with the PRISM dataset (Thornton et al. 2016) and its long length of record (early twentieth century to the present). Drought was defined as meteorological drought, based on the standardized precipitation index 3-month (SPI-3) (Hayes et al. 1999). SPI-3 is a simple statistical-based index that evaluates how anomalously wet or dry the previous 3 months were compared to climatology and, through standardization, can be properly compared across regions with notably different climates. Here we fit the gamma distribution to raw precipitation data to compute SPI-3. To analyze covariability between precipitation and large-scale circulation, the daily precipitation rate from MERRA-2 was also analyzed from the variable M2CORR. This variable is the observation-corrected version of MERRA-2 precipitation, and was analyzed due to its reduced uncertainty over land (Reichle et al. 2017) and its dynamical consistency with the atmospheric circulation conditions being analyzed in this study.

Ridging variability was investigated in relation to various remote drivers in both the tropics and high latitudes including ENSO, tropical SSTs in the western Pacific region, the Pacific meridional mode (PMM), the MJO, the Arctic Oscillation (AO), and sea ice extent variability. ENSO indices included in our analysis were the equatorial Southern Oscillation (SOI-EQ) and the Niño-3.4 and Niño-4 indices. The SOI-EQ represents the large-scale zonal atmospheric response to ENSO, defined as the standardized anomaly of the mean sea level pressure difference between regions in the western and eastern equatorial Pacific. The Niño-3.4 (5°N–5°S, 170°–120°W) and Niño-4 (central equatorial Pacific; 5°N–5°S, 160°E–150°W) indices detail tropical Pacific SST variability related to ENSO. A further SST region of interest was defined, based on SSTs in the western Pacific region (SST-WP), calculated as the linearly detrended area-weighted monthly mean standardized SST anomaly (0°–20°N, 120°–150°E). The PMM is the leading mode of non-ENSO coupled ocean-atmosphere variability in the Pacific basin (Chiang and Vimont 2004; Amaya 2019), defined by applying maximum covariance analysis (MCA) to detrended tropical Pacific SST and 10-m wind anomalies (20°S–30°N, 175°E–85°W) and with linear regression first applied to remove the concurrent ENSO influence.

The phase and amplitude of the MJO was also included in our analysis, representing the dominant component of intraseasonal atmospheric variability in the tropics. The MJO was here defined based on the commonly used real-time multivariate MJO RMM index (Wheeler and Hendon 2004). To filter out weaker MJO events, only events with an RMM index magnitude greater than 1 were considered. The AO (Thompson and Wallace 1998) is defined as the first EOF of monthly Z1000 poleward of 20°N, the positive phase of the AO is characterized by broad regions of positive Z1000 anomalies in the midlatitudes of the North Pacific and North Atlantic Oceans and negative anomalies over much of the Arctic. Correlations between monthly SST variability and ridging were also analyzed to further consider regions outside of those dominated by ENSO and MJO variability. Monthly SST data were from Centennial in situ Observation-Based Estimates 2 SST v2 (COBE-SST2; Hirahara et al. 2014). Sensitivity testing of ridging-SST correlations with an alternate SST dataset (ERSSTv5; Huang et al. 2017) revealed very similar results (not shown).

Arctic sea ice variability was analyzed from the updated HadISST v2.1 dataset (Titchner and Rayner 2014) for key regions following Swain et al. (2017): the Barents–Kara region (BK; 60°–85°N, 40°–100°E) and the Bering–Chukchi region (BC; 60°–85°N, 160°E–140°W). These regions were chosen based on a possible (but debated) causal link to California precipitation described in Swain et al. (2017) and references therein. The spatial extent anomalies of sea ice covered grid cells (where "ice covered" was defined based on grid cells where sea ice concentration >50%) were computed as anomalies from the long-term mean.

b. *Ridge detection algorithm*

The terms "ridging" and "blocking" cover a diverse range of synoptic patterns and a number of definitions

have emerged in recent years (Woollings et al. 2018). These indices can be broadly grouped in terms of absolute (e.g., Woollings et al. 2008; Davini et al. 2012; Masato et al. 2013) or departure fields (e.g., Dole 1986; Renwick 2005; Parsons et al. 2016; Liu et al. 2018). Two-dimensional absolute approaches tend to give focus to Rossby wave breaking that recognize blocking as a high–low dipole with reversed meridional gradients of geopotential height across the mid- to high latitudes. In contrast, departure methods [sometimes referred to as persistent positive anomalies (PPA)] define blocking more broadly in terms of persistent departures above the time-mean geopotential height field to emphasize the broad anomalous two-dimensional area of the blocking high.

For the purposes of this study, we carried out an initial examination of which approach to defining blocking/ridging (i.e., blocking defined based on absolute or departure fields on daily data) was most relevant to precipitation deficits over monthly and longer time periods over the western/southwestern United States. This initial analysis (not shown) revealed that blocking defined from PPA was more strongly associated with meteorological drought across this region compared to absolute approaches based on reversed meridional gradients of geopotential height in the mid- to high latitudes (e.g., Davini et al. 2012). On the basis of this, we implemented a PPA-based approach to define drought-relevant ridge events. Compared to traditional PPA-based approaches, which typically consider grid cells on an individual basis (e.g., Renwick 2005; Parsons et al. 2016), we identify spatial ''objects'' in the Z500 field based on a set of criteria in our ridge detection algorithm. In particular, we detect Z500 anomalies greater than 50 m (and separately as 100 m for sensitivity testing) and define ridge objects based on whether adjacent connected 2D grid cells are connected above a total area threshold. Only ridge objects with an area greater than 125 000 km^2 (the equivalent of approximately 50 MERRA-2 grid cells, depending on latitude) were considered to remove relatively small and isolated ridge events.

In general, the ridge detection algorithm was implemented without first detrending the input Z500 data. However, thermal expansion related to warming of the lower troposphere can lead to trends in geopotential height on constant pressure surfaces, which can complicate the interpretation of circulation trends (Horton et al. 2015; Swain et al. 2016). As a result of this, we carried out sensitivity testing to first removing the seasonal hemispheric-mean Z500 trend from each grid cell prior to running the ridge detection algorithm (e.g., Horton et al. 2015). This additional analysis allowed examination of the extent to which observed trends in the frequency of ridging events are influenced by thermal expansion of the lower troposphere. The ridge detection algorithm was implemented for October–March over a domain spanning the eastern North Pacific Ocean and the west coast of North America (domain: 20°–60°N; 190°–260°E; Fig. 1b). To target specific geographical domains of interest, an additional set of ridge detection criteria are described in the following paragraph.

To ensure the relevance of ridging events to precipitation deficits across the western/southwestern United States, we separately performed a combined empirical orthogonal function (EOF) analysis between daily precipitation anomalies and daily Z500 anomalies across the region (Fig. 1a). The EOF analysis aims to identify the main regions of positive geopotential height anomalies associated with precipitation deficits across the region (Fig. 1a). Daily precipitation anomalies were analyzed over land only for the western/southwestern United States (west of 255°E; see Fig. 1a). Before input into the combined EOF, the precipitation and Z500 fields were first normalized by both their variance and spatial extent (and weighted by latitude) such that variability in each field contributes equally to the combined vector (e.g., Wheeler and Hendon 2004).

The EOF analysis is used in the first step of the ridge detection algorithm to define the regions (Fig. 1b, boxed regions) and ridge types output from the ridge detection algorithm, which are hereafter referred to as North- (N-), South- (S-), and West-/offshore- (W-) ridge types. As shown in Fig. 1a, different patterns of positive geopotential height anomalies (contours) relate to spatial variability in precipitation deficits across the region (brown shading). The N-ridge type is associated with a positive Z500 anomaly broadly centered over Washington and related to EOF1 (40°–55°N, 225°–250°E). The S-ridge type relates to both EOF2 and EOF4 which display different configurations of ridging both centered broadly over Southern California and Arizona (28°–40°N, 235°–255°E). Last, the W-ridge type is centered offshore from California (28°–40°N, 210°–235°E). From these domains, the N-ridge type is formally defined on a given day when 1) the intensity-weighted centroid of the ridge is located anywhere in the N box region of Fig. 1b and 2) the positive anomaly defined by the ridge covers at least 50% of the N boxed region (and analogously for the S- and W-ridge types). The second condition further ensures the removal of relatively small ridge events with large gradients in Z500.

One advantage of feature tracking through the ridge detection algorithm is the detailed descriptive statistics of ridging provided at each time step, in contrast to weather-typing approaches (e.g., through self-organizing maps or *K*-means clustering; Gibson et al. 2017) that typically only provide cluster assignment. The ridge detection

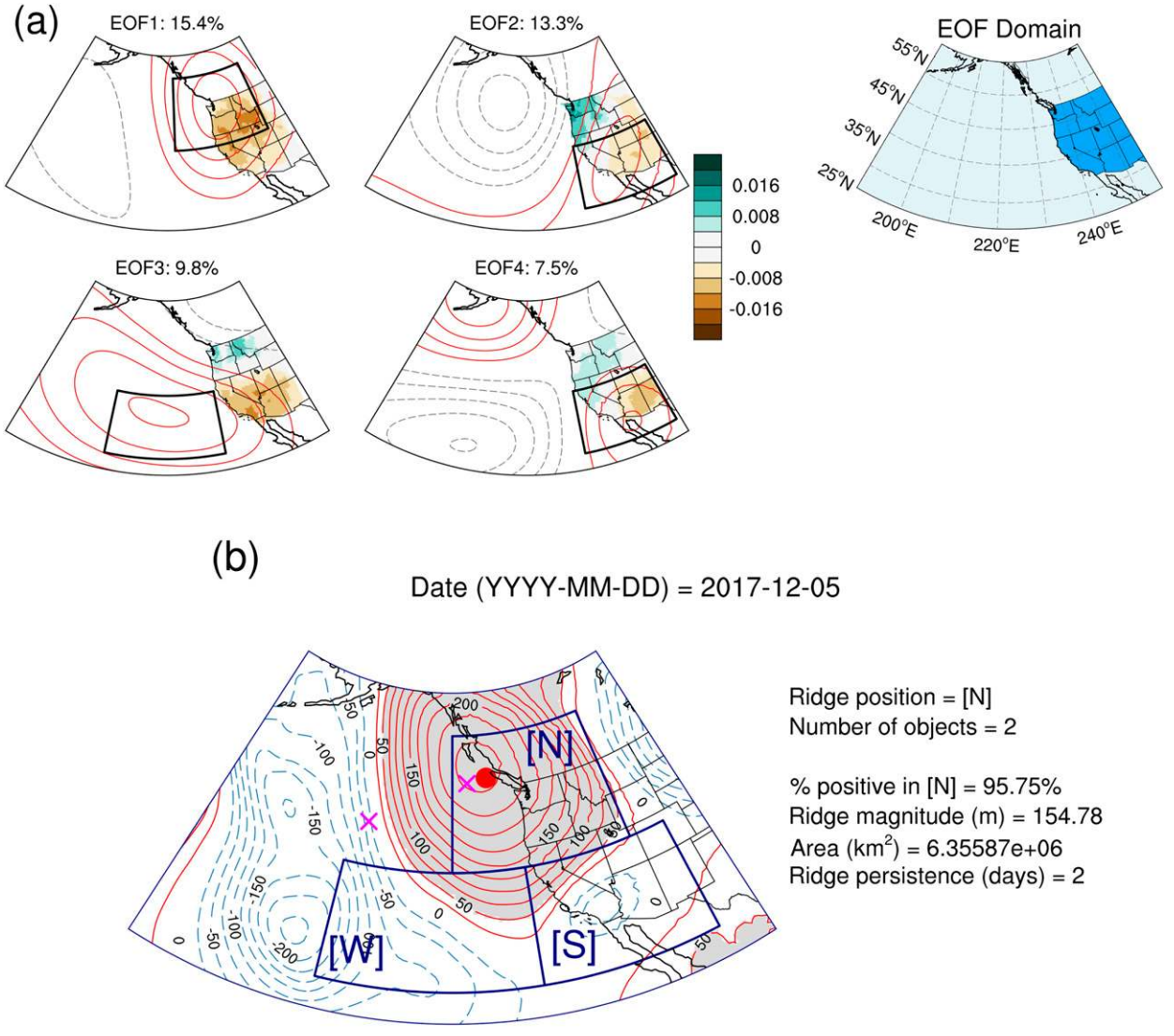

FIG. 1. (a) (left),(center) The first four EOF loadings corresponding to a combined EOF of daily precipitation anomalies over land over the western/southwestern United States (shading) and Z500 anomalies (contours); see section 2b for further details. (right) The EOF domain detailing the regions used in the combined EOF analysis for Z500 (light-blue shading) and precipitation over the western/southwestern United States (blue shading). (b) Details of the ridge detection algorithm used in this study, showing an example on a given day from MERRA-2. The three labeled boxes (N, S, W) are related to EOFs as follows: N-ridge box from EOF1 (40°–55°N, 225°–250°E), S-ridge box from EOF2 and EOF4 (28°–40°N, 235°–255°E), and W-ridge box from EOF3 (28°–40°N, 210°–235°E). Contours show the daily Z500 anomalies at 25-m intervals while the gray shaded regions indicate individual ridge objects (>50-m threshold). The red circle in (b) shows the ridge centroid for the date given, while smaller magenta crosses show the ridge centroid on the previous 2 days. Descriptive statistics show a subset of those generated by the ridge detection algorithm on a per-day and per-object basis.

algorithm outputs various statistics on a per-day and per-object basis including centroid location, magnitude (Z500 anomaly averaged across object), area, and persistence. Persistence is defined (in days) when the centroid of the ridge object persists within a particular boxed region across consecutive days, without requiring the 50% spatial criteria on each consecutive day.

Our approach to identifying spatial objects in the Z500 field is similar to the recent approach of Liu et al. (2018), but is specifically tailored toward ridge-influenced precipitation deficits over the region of interest through the combined EOF analysis step. A secondary advantage of the EOF analysis step is that for monthly/seasonal counts of ridging events we find that pairwise correlations (e.g., N-ridge monthly frequency correlated with S-ridge monthly frequency) are typically weak. The strongest of these correlation pairs (over the period 1950–2014) is Pearson's correlation coefficient $r = -0.25$

between the N-ridge type and the S-ridge type, whereas the N–W and S–W pairs have correlations of −0.12 and 0.09, respectively. While the combined unrotated EOF analysis ensures independence on a daily basis (by construction through the orthogonality of the EOF modes), this result on a monthly basis highlights that the N-, S-, and W-ridge types can also be considered somewhat independent on longer time scales. This is beneficial for ensuring that the inclusion of multiple ridge types can help explain important aspects of ridging variability related to precipitation deficits.

c. Statistical methods

A multiple linear regression analysis was carried out between SPI-3 (predictand) and the concurrent 3-monthly ridge frequency anomalies as predictors (i.e., how often each daily ridge type occurs in a given 3-month period compared to climatology). Regression models were fit on a per-region basis for region-averaged SPI-3 from Washington (WA), Oregon (OR), California (CA), Arizona (AZ), and the Colorado River basin spanning the upper and lower catchments (CO-basin). This analysis was carried out to determine which ridge types are most strongly associated with meteorological drought in different regions and to determine whether similar relationships between ridging and precipitation deficits on the synoptic time scale (i.e., daily) hold for longer drought-relevant time scales (i.e., 3-monthly). The frequency of AR events, expressed as an anomaly at each grid cell and then averaged over each of the above regions, was also included in the regression analysis. For this purpose, ARs were computed from NCEP–NCAR reanalysis over the period 1950–2014, given the extended length of record in this reanalysis product as implemented in the AR studies of Guan and Waliser (2015) and Cook et al. (2018). Since a reasonable proportion of the variability in AR frequency is expected to be explained by the variability in ridging frequency, we were primarily interested in the residual AR influence on drought. As such, the inclusion of ARs into the regression models was done in a two-step process. First, the relationship between ARs (predictand) and ridging (predictors) was assessed through multiple linear regression. Second, the difference between ARs predicted by the regression model in step 1 and the observed AR occurrence (i.e., the AR residuals) was input into the regression models as an additional predictor variable as follows:

$$\text{SPI-3}_{\text{region}} = aN + bS + cW + d(\text{AR residual}),$$

where a, b, and c are the standardized regression coefficients corresponding to the N-ridge-type, S-ridge-type, and W-ridge-type 3-monthly frequencies, respectively. The d standardized regression coefficient corresponds to the AR residual term described above.

Trends were computed for the monthly frequency and persistence of ridging conditions, carried out across different reanalysis and time periods to examine the sensitivity of trends to these factors. Trends were computed with the Mann–Kendall (MK) test with Sen's slope, which are robust to outliers and assumptions of normality. The presence of strong autocorrelation in a time series is known to influence the probability of the MK test detecting a significant trend (Kulkarni and von Storch 1995; Yue et al. 2002). To account for this, following the approach of Kulkarni and von Storch (1995), we prewhiten the time series before trend calculations by removing the lag-1 serial correlation coefficient. When plotting trends and correlations on a map, the false discovery rate (FDR) approach to significance testing was implemented, following Wilks (2016). This approach reduces the likelihood that the null hypothesis is incorrectly rejected through multiple hypothesis testing. Correlations were calculated from linearly detrended data to reduce the risk of spurious correlation arising from co-occurring but unrelated trends.

Associations between MJO phase and ridge frequency anomalies were computed as a function of lag in days following strong MJO events (section 2a). We compare the frequency of ridge occurrence under MJO phase with the typical frequency of ridge occurrence under ''all conditions'' expressed as a relative percent difference. To assess significance of these ridging anomalies, we follow a similar approach to Henderson et al. (2016) and implement a moving blocks bootstrap for each lag/phase. This approach samples elements from the original dataset (with replacement) by blocks of size l repeated 10 000 times to obtain sufficient bootstrap samples. Similar to Henderson et al. (2016), we implemented a fixed $l = 6$, as results were found to be insensitive to other reasonable choices of l (e.g., l = 4–6 and allowing l to vary by MJO phase; not shown).

3. Results

a. Ridging and precipitation deficits

A major goal of this study is to characterize ridge types that are directly relevant to precipitation deficits (across a range of temporal scales). Therefore, we begin by examining and quantifying how ridging (the three ridge types identified in Fig. 1 and described in section 2b) can influence ARs, precipitation, and meteorological drought from a climatological perspective. The conditional probability of AR occurrence given ridge occurrence (N-, S-, W-ridge types) in terms of relative risk is

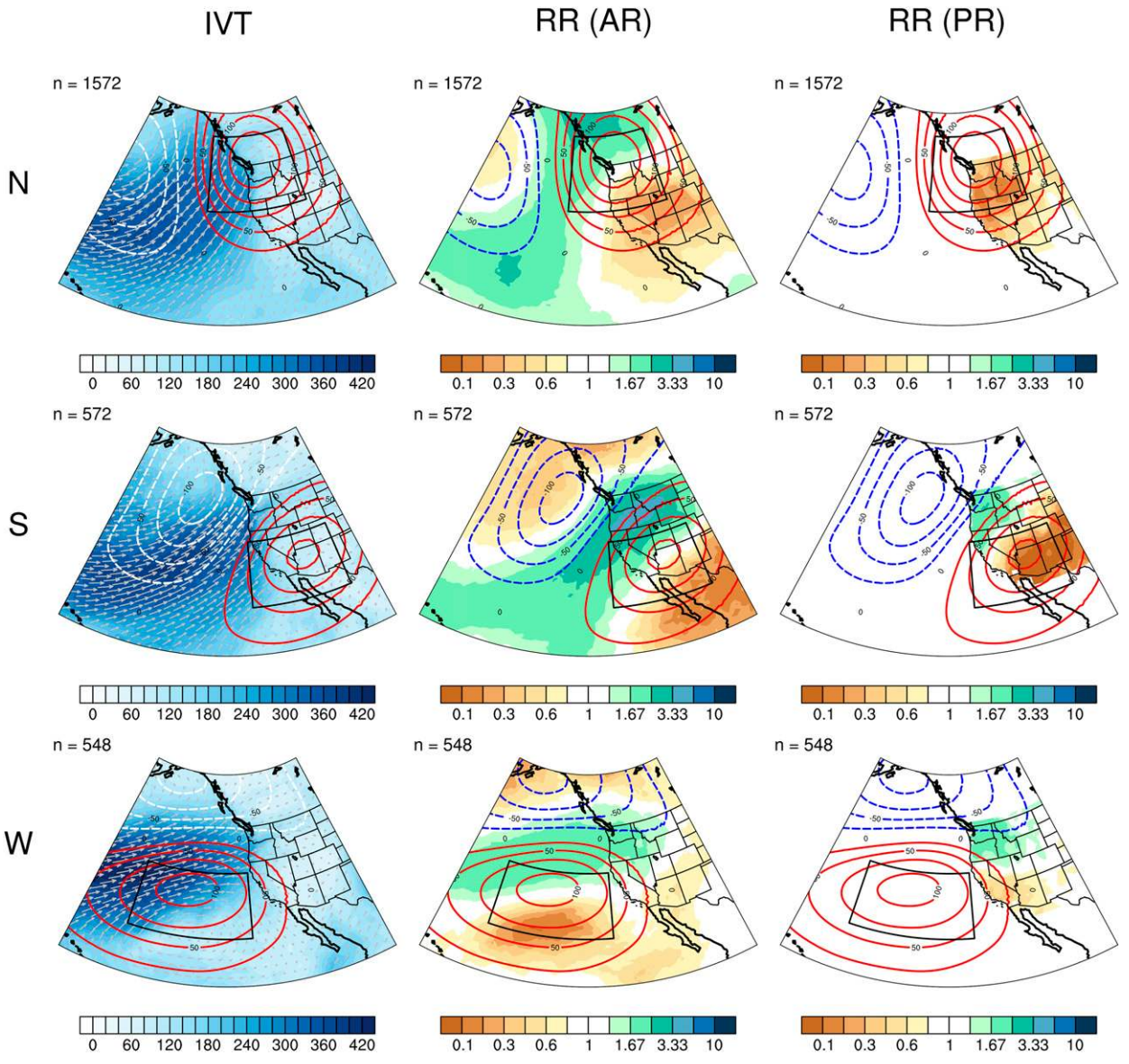

FIG. 2. (left) Mean 6-hourly AR-related IVT vectors and magnitude (shading) given ridge occurrence for each ridge type: N, S, and W. (center) Relative risk (RR) of AR occurrence given ridge occurrence. A relative risk value less than 1 indicates a decreased likelihood of AR occurrence given ridge occurrence. (right) RR of a precipitation-day occurrence given ridge occurrence. Here a precipitation day is defined as a day with precipitation greater than the monthly long-term climatology at that grid cell, defined for grid cells over land only. Data are from MERRA-2 with the sample size of ridge occurrence (days) shown above each panel.

shown in Fig. 2 (center column). A lower (higher) value of relative risk indicates a lower (higher) probability of AR occurrence given ridge occurrence, compared to the probability of AR occurrence in the absence of ridge occurrence. As shown in Fig. 2, the N-ridge type (top row) substantially reduces the likelihood of ARs making landfall across a broad region spanning Northern California, Washington, and Oregon and also reduces the likelihood of inland-penetrating ARs across the entire American West. Over Northern California and Oregon, relative risk (RR) values can reach ~0.2 indicating a roughly five-fold reduction in AR landfall likelihood under the N-ridge type. The N-ridge type tends to divert ARs northward, as indicated by the direction of IVT and the positive values of AR relative risk across British Columbia and Alaska. For ridging centered more directly over the Southwest under the S-ridge type (middle row), a reduction in AR likelihood is found for southern portions of the interior Southwest, including Arizona and New Mexico. The S-ridge type also tends to divert ARs

northward to strongly increase the likelihood of AR occurrence over Washington and Oregon. Last, the W-ridge type (bottom row), which is centered farther offshore from California, tends to reduce AR likelihood across California and Arizona, where it decreases AR likelihood by more than a factor of 2 (relative risk < 0.5). Collectively, these results show that each of the three defined ridge types (N-ridge, S-ridge, and W-ridge types) can play a role in deflecting ARs from California, highlighting that multiple ridge types can be important for influencing precipitation in an individual region.

It is important to note that not all precipitation is AR-related, and that the importance of ARs for precipitation differs between regions. To address this, the right column of Fig. 2 displays the RR of a precipitation day given a ridge occurrence. A precipitation day is defined here as a day where the daily precipitation total exceeds the long-term precipitation climatology (defined with respect to the month of year) at that grid cell, calculated for grid cells over land. Broadly similar relationships with ridging are found for precipitation days compared to AR occurrence, highlighting a robustness in how ridging influences both of these quantities. For the S-ridge and W-ridge types, the RR of precipitation days less than 1 (brown shading) extends across a wider domain across the Southwest (compared to the RR of AR days less than 1). This highlights the importance of both these ridge types for influencing precipitation deficits across a wide region spanning Southern California and most of the Colorado River basin in the interior Southwest, and indicates the relevance of these ridge types for also influencing precipitation deficits that are not AR-related. As was found for the RR of AR days, the N-ridge type remains important for all Pacific coast states. Also notable is the increased likelihood of precipitation over Washington and Oregon (and parts of Northern California) under S- and W-ridge-type occurrences, consistent with how these ridge types relate to AR landfall likelihood described above.

We next examine relationships between ridging and precipitation and meteorological drought over longer time scales (i.e., beyond the synoptic time scale associated with individual ridges/waves). This analysis is carried out on a per-region basis in Fig. 3, since the relationships between ARs and precipitation were shown in Fig. 2 to be strongly regionally dependent. We also include the Colorado River basin in our analysis given its importance to water resources across the western states. Figure 3 shows the regression coefficients from fitting multiple linear regression models between SPI-3 (predictand) and the concurrent 3-monthly ridge and AR occurrence (predictors) for each region. A positive and statistically significant regression coefficient (orange shading) indicates ridge types that are most strongly (and positively) associated with drought in the different regions. In broad agreement with the earlier findings from the perspective of daily ARs and precipitation (Fig. 2), the N-ridge type is found to be positively associated with meteorological drought across WA, OR, and CA. Notably, in CA the S-ridge and W-ridge types also are positively associated with drought, highlighting the diverse pathways for CA to enter into drought from a ridging perspective. For AZ and CO-basin, both the S-ridge type and W-ridge types are positively associated with drought periods. Additionally, the AR term is significant and negative in all regression models, highlighting the importance of both ridging and ARs for explaining drought variability across these regions. It is important to note that the AR term in the regression models of Fig. 3 is a residual term (formed from the residuals of the relationship between ARs and ridging, see section 2c), highlighting that the influence of ARs on drought cannot be explained solely through the influence of ridging. As shown earlier in Fig. 2 at the daily time scale, not all ridge types in Fig. 3 are positively associated with drought in all subregions (orange shading), with the S-ridge type reducing the likelihood (blue shading) of drought over Washington and Oregon.

A similar role, in terms of how each ridge type influences precipitation deficits in different regions, was found when examined over shorter monthly periods for SPI-1 (Fig. S2). The broad consistency in terms of how these ridge types each influence regional ARs and precipitation deficits on daily time scales (Fig. 2) through to monthly and 3-monthly time scales for SPI-1 and SPI-3 (Fig. 3) provides confidence in the general robustness and drought relevance of these associations, as well as the usefulness in discriminating between the different ridge types for understanding drought.

b. Ridge climatology and trends

We next explore the general climatology (i.e., ridge frequency, magnitude, area, and persistence) and long-term trends for each of the three ridge types. As shown in Fig. 4a, the frequency of ridge types (in terms of percentage of frequency of occurrence across all days between 1950 and 2014 and October–March) can display a relatively large amount of variability between months. Typically, the N-ridge is the most common ridge type, followed by the W- and S-ridge types. The W-ridge-type frequency on average peaks later in the season (January–March) around when the N-ridge type is on average least frequent. However, as shown in Fig. S3, individual months or years can deviate substantially from this typical monthly frequency climatology. Given the variability in ridging frequency between months, the long-term frequency by month is removed from the monthly ridge frequency in subsequent analysis (which we refer to

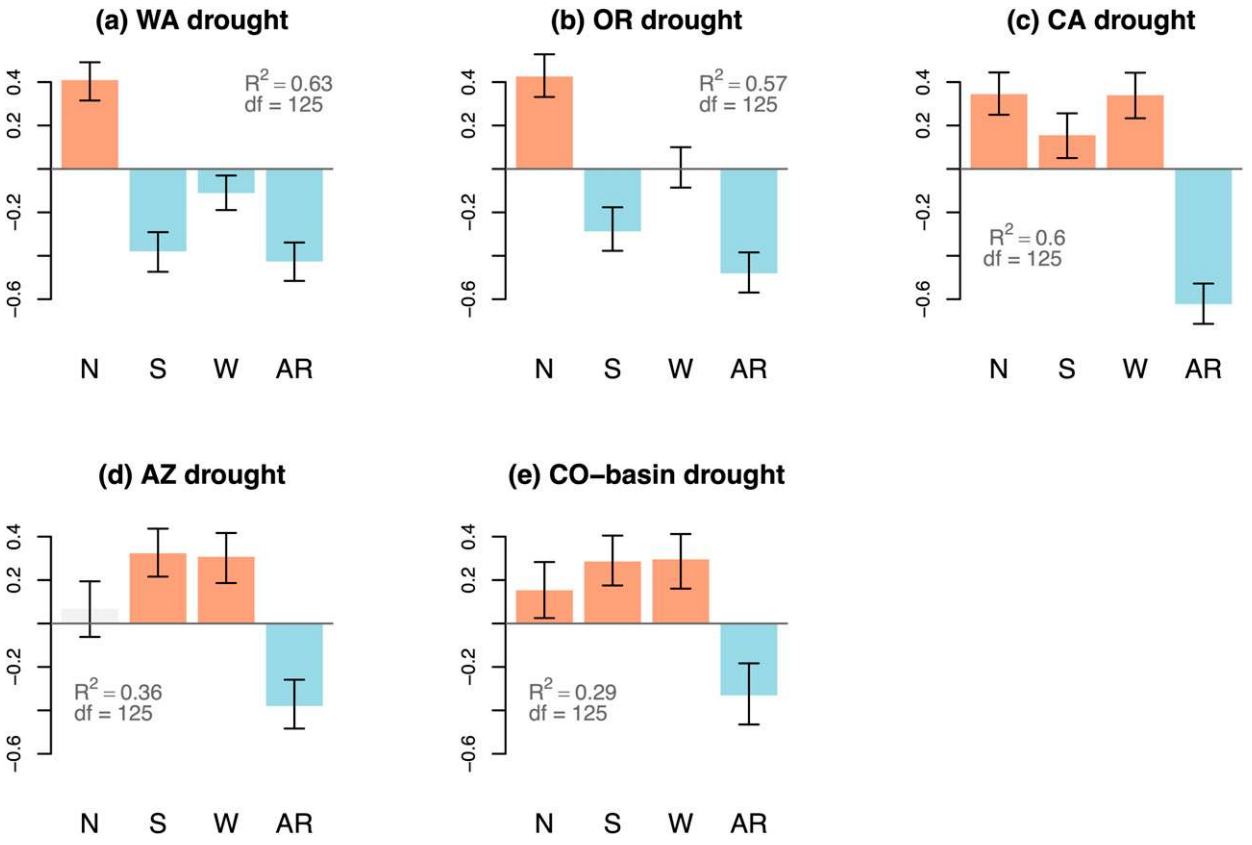

FIG. 3. Standardized regression coefficients from a multiple linear regression between SPI-3 in each region and the N-, S-, and W-ridge-type 3-monthly occurrence frequency over the period 1950–2014. The AR term represents the residual AR contribution to SPI-3 variability after accounting for the relationship between ridging and ARs (see section 2c for details). Shading indicates significance of coefficient (based on bootstrapping with $R = 1000$) such that orange bars indicate which ridge types are most strongly associated with drought variability in each region. The R^2 values of the regression model and the degrees of freedom (df) are also shown. Ridge-type frequencies were generated from 20CRV2c.

as monthly ridge frequency anomaly). In terms of the magnitude of Z500 anomalies averaged over ridge objects (Fig. 4b) the N-ridge type has the highest median Z500 magnitudes (around 120 m) compared to the S- and W-ridge types. The average magnitude of the anomalies shows relatively little between-month variability; however, all ridge types show a peak in magnitude for January–February months (Fig. S3). The N-ridge type tends to persist for longer than the other ridge types (Fig. 4d); although the median persistence is 2 days, the distribution of ridge persistence is heavily skewed with a number of events showing persistence greater than 10 days. The average persistence of all ridge types is also typically larger across January–February (Fig. S3). In terms of spatial area spanned by ridge objects, the differences between ridge types are relatively small with a large amount of within-group variability. Very similar results were obtained for the general ridge characteristics when analyzed in ERA-Interim and MERRA-2 (not shown).

Trends in the monthly ridge frequency anomaly are examined in Figs. 5 and 6, including testing the sensitivity of trends to different reanalyses (20CRV2c, MERRA-2, and ERA-Interim), time periods, and the influence of thermal expansion. As shown in Fig. 5, significant long-term trends in ridge frequency from 20CRV2c over the period 1950–2014 are not evident, with a large degree of interannual variability in ridge frequency. A similar lack of significant trends is observed for ridge persistence over this period, where persistence is defined as the number of days spanned by the longest sequence among all ridge sequences in a given month (Fig. S4). Over the shorter postsatellite period (e.g., 1980–2017 in Figs. 5 and 6) trends in both frequency and persistence are typically also weak and nonsignificant.

The notable exception is for the S-ridge type, with a slight positive trend in both frequency and persistence observed across both MERRA-2 and ERA-Interim, emerging only in the more recent postsatellite period (e.g., from 1980 onward; Fig. 6). Further analysis of this

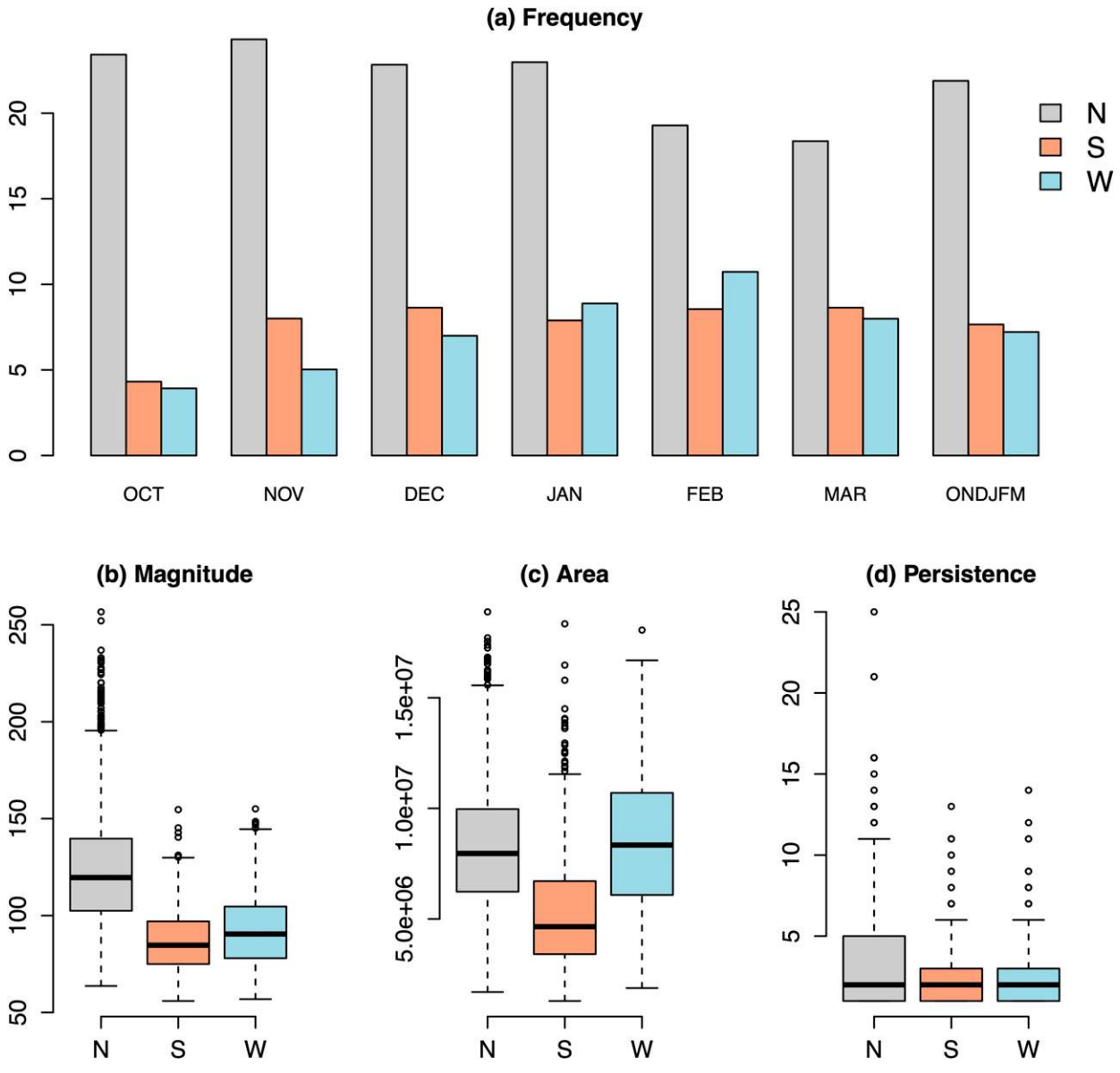

FIG. 4. Distributions of ridge characteristics for N-, S-, and W-ridge types: (a) frequency (percentage occurrence from all time steps), (b) magnitude (m), (c) area (km^2), and (d) persistence (days). These characteristics were generated from 20CRV2c over the period 1950–2014 for months October–March. Boxplot components are horizontal line (median), boxes [interquartile range (IQR)], whiskers (1.5IQR), and outliers/circles (> 1.5IQR).

S-ridge-type trend (Fig. S5), computed over individual months, reveals that positive trends in frequency and persistence are largely driven by the shoulder season months of October and March, and to a lesser extent February (as opposed to November–January).

When a larger anomaly threshold is applied in the ridge detection algorithm (100-m threshold instead of 50 m; Fig. S6) the largest trends are also observed for the S-ridge-type frequency and persistence, while other ridge types show no evidence of an upward trend over this period. When the 100-m threshold is applied, the S-ridge frequency trend magnitude and significance are reduced in both MERRA-2 and ERA-Interim, although this trend remains significant for the S-ridge persistence. This suggests that the S-ridge frequency trend (Fig. 6) is more driven by an increase in the frequency of relatively small magnitude ridging anomalies (>50 m) as opposed to large ridging anomalies (>100 m). Sensitivity testing of detrending Z500 prior to running the ridge detection algorithm (Fig. S7) also allowed examination of the extent to which thermal expansion may have influenced the S-ridge frequency and persistence trends. As shown,

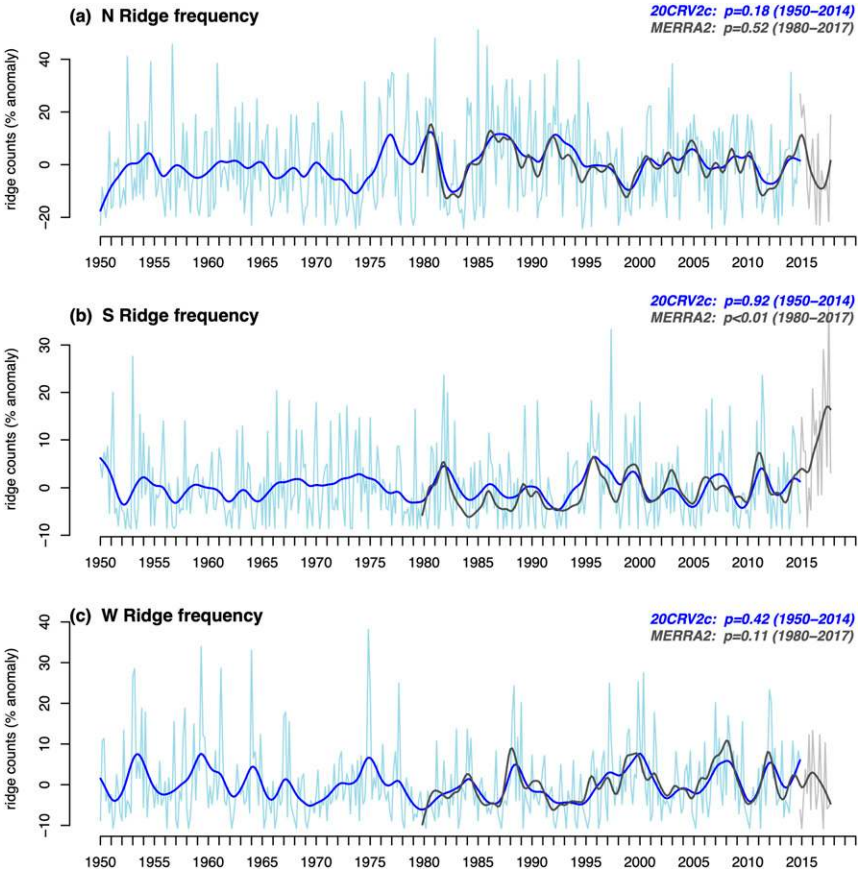

FIG. 5. Time series of monthly ridge frequency occurrence anomaly for each ridge type—(a) N, (b) S, and (c) W—for 20CRV2c (blue line; 1950–2014) and MERRA-2 (gray line; 1980–2017). Mann-Kendall trend p values are given for each reanalysis across the relevant time periods, computed on the monthly data (October–March). The thicker line for each reanalysis is a fitted cubic spline showing lower-frequency variability. To aid visualization, MERRA-2 at the monthly frequency is only shown after 2015.

removing the direct influence of thermal expansion reduces the magnitude of the S-ridge type frequency and persistence slightly, however both trends remain positive and strongly statistically significant ($p < 0.05$).

Although there are some differences in ridge frequency between reanalysis products in individual months, these become less pronounced in the smoothed running mean and illustrate a general consistency between reanalysis. These differences are considerably smaller between MERRA-2 and ERA-Interim (Fig. 6) compared to between MERRA-2 and 20CRV2c. This likely reflects the reduced set of observational data assimilated in 20CRV2c (only surface observations of synoptic pressure, monthly SST, and sea ice are assimilated) that adds uncertainty at the 500-hPa level.

c. *Remote drivers and predictability*

We next explored various remote drivers and sources of predictability for the different ridge types, on the basis that these may help facilitate longer lead prediction into S2S time scales. Concurrent correlations (i.e., at zero lag) between monthly ridge frequency anomalies and gridded SST anomalies, geopotential height anomalies (Z500) and zonal wind anomalies (u200) over October–March months for the period 1950–2014 are shown in Fig. 7. The N-ridge-type correlation with both Z500 and u200 displays a wave train pattern with apparent links to the central tropical Pacific. Remote correlations between the N-ridge and SST are fairly weak for October–March; however, a more localized positive–negative SST correlation dipole is found along the wave train pattern of the Z500 correlations. Furthermore, for the latter half of the water year (i.e., January–March; Fig. S8), a stronger positive correlation between the N-ridge type and tropical SSTs is observed just west of the international date line. The S-ridge-type correlation with Z500 and u200 displays a wave train pattern that appears to be driven more from the mid- to high latitudes with little tropical forcing.

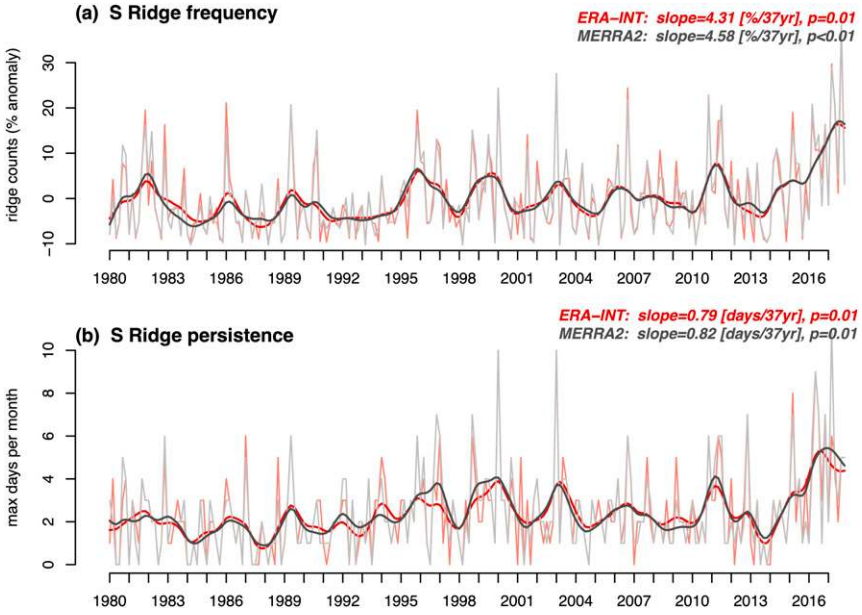

FIG. 6. As in Fig. 5, but for (a) monthly ridge frequency and (b) monthly ridge persistence for MERRA-2 (gray line) and ERA-Interim (red). Persistence is defined as the number of days spanned by the longest sequence among all ridge sequences in a given month. The S-ridge-type frequency for MERRA-2 in (a) is identical to that in Fig. 5b.

The S-ridge type also has very weak correlations with remote SSTs in support of the lack of a consistent tropical forcing. The W-ridge type has a stronger relationship to tropical SST compared to the S- and N-ridge types. In particular, months with a higher-than-normal W-ridge-type frequency are associated with cooler-than-normal SSTs in the central tropical Pacific and warmer-than-normal SSTs in the western tropical Pacific and subtropics, somewhat similar to a La Niña–like–Pacific decadal oscillation (PDO) pattern. This association is similar, but with stronger correlation strength, when only January–March are analyzed (Fig. S8), suggesting that the response becomes stronger later in the season. The Z500 correlation with the W-ridge type is also broadly consistent with the typical Z500 response to La Niña, where the associated ridge is positioned some distance offshore from California (e.g., Garfinkel et al. 2012). The u200 correlation with the W-ridge-type frequency is also consistent with the typical poleward shift and weakening of the winter Pacific jet stream during La Niña compared to El Niño (e.g., Seager et al. 2005).

Lagged correlations between monthly ridge frequency anomalies and gridded SST anomalies and gridded Z500 anomalies are shown in Figs. S9 and S10. Analyzing SST and Z500 anomalies in the months preceding ridge frequency anomalies provides further indication of which remote drivers offer extended opportunities for longer-lead predictability. For the S- and W-ridge types, similar coherent signals in tropical SSTs are also observed at 1- and 2-month lead times. However, for the N-ridge type, the more localized positive SST correlation along the U.S. West Coast shown in the concurrent correlation is diminished at longer leads. This implies that local SSTs in this region are not a necessary precursor to months with strong ridging, at least on monthly time scales, but that remote (tropical) SST may indeed be predictive of S- and W-ridge-type occurrences 1–2 months in advance. As expected, given the more limited memory in the atmosphere compared to SSTs, Z500 correlations are typically much weaker (and not statistically significant) at longer lead times.

The association between ridge type frequency and a wider range of potential remote drivers/modes of variability (i.e., spanning both tropical and latitude drivers) is investigated in Fig. 8 (and in Fig. S11 and S12 for ridge persistence and ridge magnitude). As shown in Fig. 8, correlations are typically found to be stronger in the second half of the water year (January–March; Fig. 8b) compared to the full water year (Fig. 8a). A similar result is found when only October–December months were analyzed (not shown), suggesting a weakened potential for predictability across these months. The different ENSO and tropical SST indices also show a range of correlation strengths highlighting the importance of considering multiple indices. In particular, the N- and W-ridge types are more strongly associated with more central Pacific SSTs (Niño-4) while the S-ridge type shows stronger correlation strength with Niño-3.4. It is notable

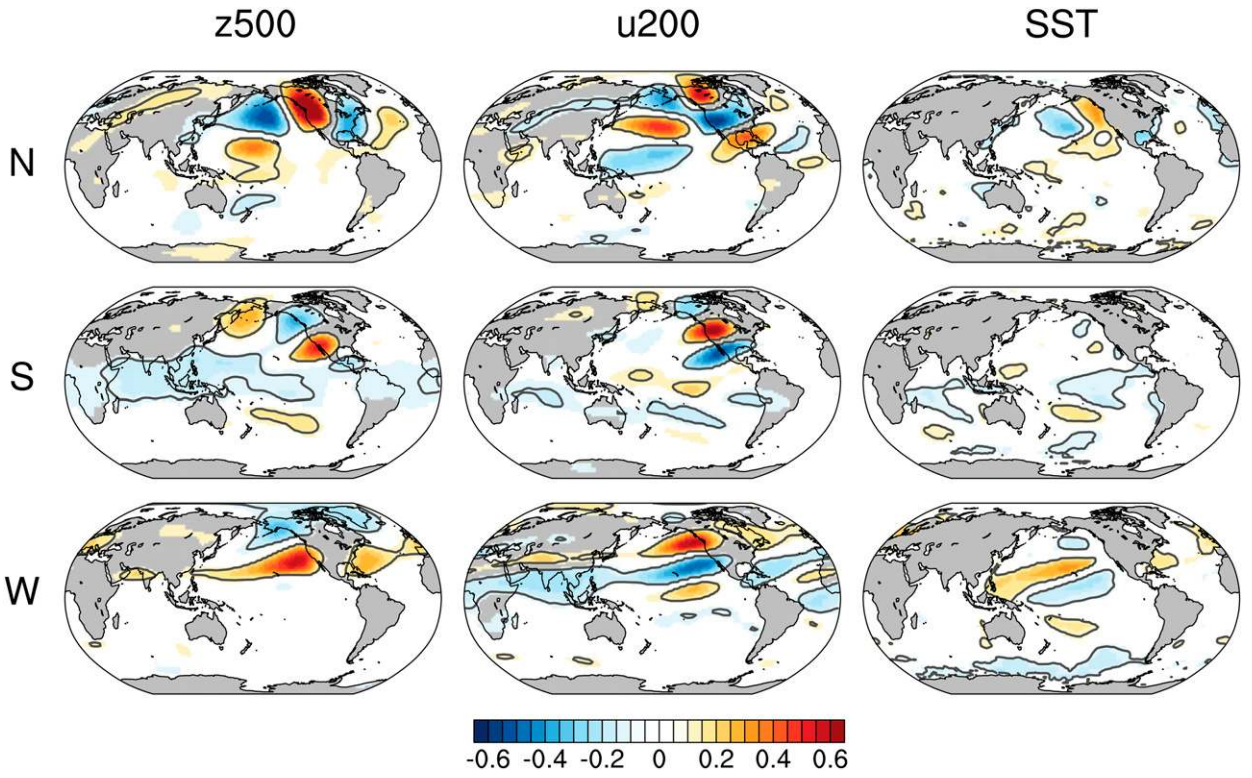

FIG. 7. Pearson correlation coeffients computed at each grid cell between monthly ridge frequency anomalies and (left) concurrent monthly Z500 anomalies, (center) concurrent zonal wind anomalies at 200 hPa (u200), and (right) monthly SST anomalies. All variables were detrended before correlation. Only local p values < 0.05 are shown and gray contour indicates FDR under $\alpha = 0.05$ (see section 2c). The time period is 1950–2014 across October–March with ridge frequencies generated from 20CRV2c. Figure S8 also shows these correlations, but across January–March only.

also that SSTs in the western tropical Pacific tend to show similar or stronger association with ridging than other ENSO indices, especially for the N- and W-ridge types across January–March (as consistent with the correlation maps shown in Fig. 7).

In terms of high-latitude drivers, sea ice variability over the Bering–Chukchi (BC) and Barents–Kara (BK) region were generally found to be only weakly associated with ridging during most calendar months (October–March). However, we do find increased correlation strength and statistical significance with the W-ridge-type frequency from January to March. The AO is also shown to be only associated with the W-ridge type frequency. In summary, the high-latitude drivers examined here appear to primarily only influence the W-ridge type (mostly in the latter half of the water year), whereas tropical drivers also tend to show the strongest associations with the W-ridge-type frequency (relationships that are present throughout the water year but are stronger in the latter half).

The association between remote drivers/modes of variability and ridge magnitude and persistence is shown in Fig. S11 and S12. Compared to ridge frequency, the ridge persistence and magnitude show similar but typically weaker associations with all three ridge types. Exceptions to this are for the association between the W-ridge-type magnitude and sea ice over the BK region and for the S-ridge-type magnitude and sea ice over the BC region, both of which show slightly stronger (negative) correlation strength and significance compared to the ridge frequency correlations (Fig. 8). This offers some modest observational evidence for the hypothesis that certain high-latitude drivers may (in some specific ridging cases) module the strength/amplitude of pre-existing wave patterns, rather than triggering them outright.

Another potential source of predictability for ridging on S2S time scales is through the MJO. Figure 9 shows the relative difference in ridging frequency during various phases of strong MJO events and lag times. This analysis shows that certain MJO phases can amplify the probability of ridging conditions across several weeks (i.e., out to 24 days) after the MJO event, with associations typically strongest for the W-ridge type. In particular, MJO phases 3–6, associated with MJO convective anomalies from the western Maritime Continent through to the central Pacific Ocean, are related to an increase in the

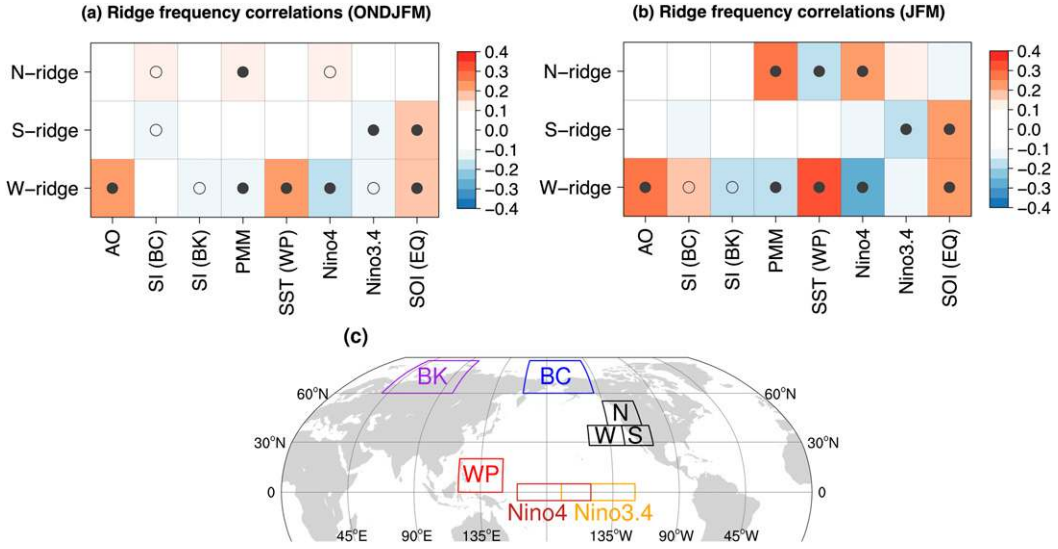

FIG. 8. Pearson correlation coefficients between monthly ridge frequency anomalies and various remote drivers/modes of variability (x axis): the Arctic Oscillation (AO), sea ice variability over the Bering–Chukchi (BC) and the Barents–Kara (BK) regions, the Pacific meridional mode (PMM), SSTs in the western Pacific (SST WP), the Niño-4 index, the Niño-3.4 index, and the equatorial Southern Oscillation index (SOI-EQ.). Correlations are shown for (a) October–March and (b) January–March; p values < 0.05 are indicated by open circles and p values < 0.01 are indicated by filled circles. The time period is 1950–2014 with ridge types generated from 20CRV2c. (c) The locations of select regions to aid interpretation. Figures S11 and S12 also show these associations, but for ridge persistence and ridge magnitude, respectively.

W-ridge frequency at longer lead times (i.e., beyond 2 weeks). For the N- and S-ridge types, the association with MJO is often mixed; however, MJO phases 4 and 5 are positively associated with these ridge types at long lead times.

For diagnostic purposes, and to shed light on the relevant dynamics in the lead-up to particularly strong and persistent ridge type occurrences, Fig. 10 shows composites of anomalous velocity potential and WAF across the ridge event life cycle. This analysis was based on a smaller set of ridging events that satisfied both of the following conditions: 1) the magnitude of the ridge anomaly was greater than the 90th percentile, defined separately for each ridge type, and 2) the positive Z500 anomaly was centered and persisted in the boxed region for 3 or more consecutive days. In Fig. 10, composites for each ridge type are separated on the basis of maturity across their life cycle: from development (t = 1–3; left column) to maturity (t = Mature, defined as the time where the above conditions are first met and until the end of event; right column).

Extreme occurrences of the N-ridge type (Fig. 10) tend to be associated with a pronounced wave train with WAF vectors emanating from a broad area near the western tropical Pacific under a region of convection (negative velocity potential anomalies during maturity). This region of convection in the western tropical Pacific region is also associated with positive precipitation anomalies (Fig. S13) in the same region and, given the location, can occur independently from ENSO events. Its relevant to point out that although this pattern is pronounced in the composite mean, not all individual events were found to have clear links to the tropics when studied individually (not shown). Extreme occurrences of the S-ridge type tend to be associated with a wave train and WAF vectors emanating from a strong ridge upstream in the midlatitudes of the western North Pacific. The wave train also tends to impact the broad BC sea ice region, which was shown earlier to be negatively correlated (albeit weakly) with the S-ridge-type frequency (Fig. 8a) and magnitude (Fig. S12). A reasonably large negative velocity potential anomaly composite is also found across the life cycle of the S-ridge type broadly spanning the Indian Ocean and Maritime Continent (though more subtropical in latitude), with a ridge over the South Asian continent marking the beginning of the downstream wave train across the Pacific. The WAF vectors for the W-ridge type are less illustrative of its typical origin, perhaps reflective a range of different configurations that can lead to extreme W-ridge occurrences, but with the broad ridge offshore of North America acting as a Rossby wave source for the development of a downstream trough–ridge pattern across North America as the W-ridge develops into maturity. The velocity potential anomalies for the W-ridge at maturity show a wide

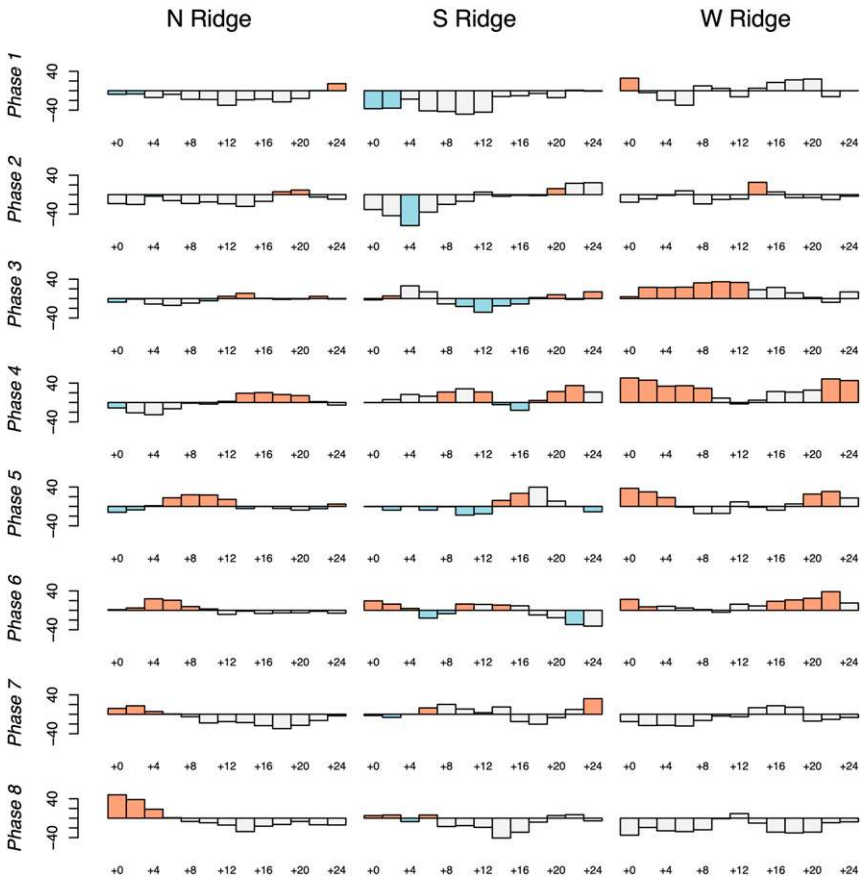

FIG. 9. Ridge frequency anomaly (*y* axis; relative/percentage difference) by MJO phase for various time lags (*x* axis; days) after a strong MJO event. Positive and negative differences that are significant at the 95% level are shaded orange and blue, respectively (see section 2c for details about significance testing). The sample size in days for each phase of the MJO at lag 0 (in order of phase from 1 to 8) is 442, 524, 585, 546, 571, 608, 610, and 506. Ridge types were generated from MERRA-2 (years 1980–2017, October–March).

region of negative velocity potential across spanning the Maritime Continent and Pacific, again likely reflecting that a range of different convective conditions can occur during extreme ridging conditions. This composite does not resemble the typical west–east ENSO dipole in velocity potential, to highlight that a range of conditions outside of ENSO can give rise to extreme ridging conditions (shown also for the precipitation anomalies in Fig. S13). All ridge types display strong negative velocity potential anomalies across various locations between the western Maritime Continent and the central Pacific Ocean, broadly consistent with the particular phases of MJO shown earlier as being important in Fig. 9.

4. Discussion

In this study, an object-based ridge detection algorithm has been developed through distinguishing particular ridge types that induce winter precipitation deficits and drought across the western/southwestern United States. Previous studies have often relied on relatively simple indices to describe ridging in this region, such as monthly or seasonal averaging of Z500 over a prescribed spatial domain. Other studies have focused on blocking and associated dynamical origins in this region (e.g., Henderson et al. 2016) but are arguably of less direct relevance to meteorological drought under the more constrained definition of blocking. In this study we first demonstrated that the three ridge types introduced here (N-, S-, and W-ridge types), separated based on centroid location of Z500 objects, have important influence on ARs and precipitation deficits. These ridge types influence precipitation deficits across a range of time scales, not just in terms of individual events and transient waves but also for meteorological drought on seasonal time scales. Notably, there is strong regionality in terms of how different ridge types influence precipitation deficits. For example, precipitation deficits across California

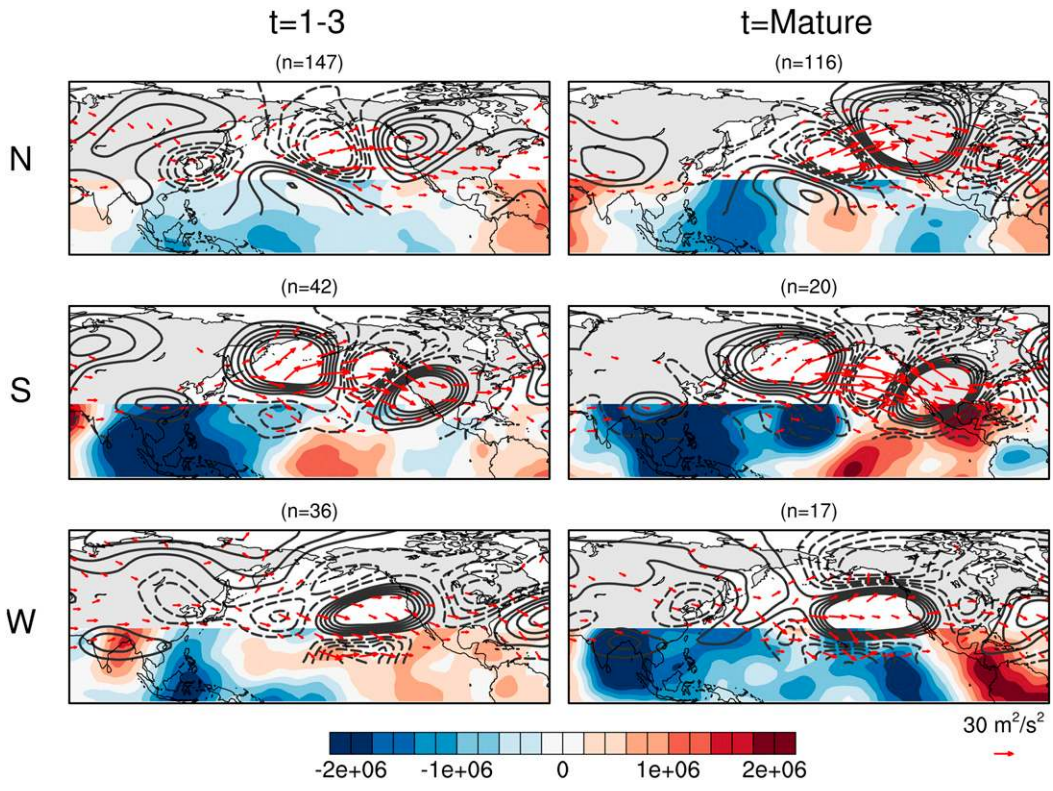

FIG. 10. Extreme ridge event composites of 250-hPa wave activity flux (WAF; vectors), 10-day low-pass-filtered 250-hPa streamfunction anomalies (positive and negative values are solid and dashed contours, respectively), and 250-hPa velocity potential anomalies (shading). Rows indicate each ridge type; columns indicate the time in days since the onset of the ''extreme event'' (see section 3c for details). The sample size *n* (days) differs between columns because of differences in how many days each ridging event persists for after reaching maturity. To aid interpretation, velocity potential is shown only for latitudes 10°S–30°N and WAF vectors are only shown for WAF $> 10\,m^2\,s^{-2}$. Extreme event ridge types were selected from MERRA-2 (years 1980–2017, October–March). Figure S13 also shows composites of precipitation anomalies under these categories.

(on monthly to 3-monthly time scales) can be influenced by all three different ridge types, which are only weakly correlated with each other over these time scales, highlighting the different ridging pathways that can facilitate drought conditions. The relatively low (and often negative) correlation between the monthly frequency of ridge types (detailed in section 2b) likely relates to the typical Rossby wavelength relative to the domain size of each ridge type—where a large positive height anomaly (i.e., ridge) in one domain is often followed by a negative anomaly (i.e., trough) downstream (e.g., Figs. 7 and 10). This relationship, while expected on daily time scales, appears to hold also for the monthly correlation between ridge types.

The finding that there are different pathways for a region to enter into drought (e.g., through a combination of ridge types) is consistent with Cook et al. (2018), who showed that seasonal ridging patterns can differ considerably between drought periods, especially in terms of the typical latitudinal position of the ridge. Furthermore, in our study, over the recent severe drought period (i.e., across winters of 2012–16) both the N-ridge and S-ridge types occurred more frequently and with more persistence than typical (Figs. 5 and 6). Notably, the N-ridge type played a more active role during much of the drought period (2013–16; Fig. 5) while the S-ridge type was considerably more frequent and persistent across the final years of the drought (2015–16 and early 2017; Fig. 6). This highlights the value of the ridge detection approach, since the details of individual ridge types are not readily identified through simply averaging over a large spatial domain or longer temporal period.

The N-ridge type presented here (Figs. 1 and 2) is most similar to the typical monthly/seasonal ridging pattern often described in previous studies as being important to drought (e.g., Seager et al. 2015; Teng and Branstator 2017; Swain et al. 2017). The N-ridge type is most relevant to Washington, Oregon, and California. In contrast, the more southern S-ridge type (centered over the Southwest) and W-ridge type (centered farther

offshore to the west) are more relevant to Southern California, Arizona, and the Colorado River basin. On monthly and 3-monthly time scales, the association between ridging frequency and meteorological drought is somewhat weaker for the Colorado River basin compared to other regions, as indicated by the goodness-of-fit statistics in Fig. 3 (and in Fig. S2 for SPI-1). This suggests that a greater diversity of synoptic conditions governs precipitation deficits in this region and future research may help in targeting and refining these conditions.

Through investigating the long-term climatology of ridge characteristics, a reasonably large degree of between-month variability was shown to exist across the water year. While it is beyond the scope of the present study to formally investigate causes of the seasonal variability in ridging characteristics (Fig. 4 and Fig. S3), we briefly discuss this here. As shown in Fig. 4, the frequency of the W-ridge type undergoes relatively large increases across the season from its climatological minimum at the start of the season (October and November) to its maximum in February. In contrast, the frequency of the N-ridge type reaches a climatological minimum late in the season (February and March). We note that the seasonal variability in ridging frequency cannot simply be a consequence of the seasonal cycle in Z500 due to the removal of the seasonal cycle when first constructing Z500 anomalies (see sections 2a and 2b). The late season changes in ridge frequency may relate to seasonal changes in the position of the North Pacific jet acting as a waveguide for the preferential formation of ridges in this region (Teng and Branstator 2017), where toward the latter half of the October–March (ONDJFM) season, the climatological North Pacific jet extension region near the U.S. West Coast shifts equatorward and a subtropical component of the jet begins to form (Newman and Sardeshmukh 1998). The fact that tropical teleconnections were shown to be stronger later in the water year (January–March vs October–December), and that these tend to preferentially impact the W-ridge type (Figs. 7 and 8 and Fig. S8), may contribute to the later season W-ridge-type maximum. Changes in the storm-track variability across the ONDJFM season (Hoskins and Hodges 2019) are also associated with larger synoptic variability across the equatorward W-ridge- and S-ridge-type regions later in the season (not shown), which may more readily give rise to anomalies that exceed the threshold for ridging.

For most ridge types and time periods, statistically significant trends in frequency and persistence were not found (Fig. 5), highlighting the large interannual variability in ridging across this region. However, the exception to this is a slight positive trend in the S-ridge type (Fig. 6) (for ridging centered broadly over the Southwest), found for both frequency [4.3%–4.6% $(37\,\mathrm{yr})^{-1}$; $p < 0.01$] and persistence [$\sim$0.8 days month^{-1} $(37\,\mathrm{yr})^{-1}$; $p = 0.01$] and further enhanced during the months of October, February, and March (Fig. S5). The higher than usual frequency and persistence of the S-ridge type in this location especially over the most recent two decades has likely partly contributed to the winter drying trend over parts of the Southwest over this season and time period (see Fig. S14). Evidence in support of this comes from how the S-ridge type substantially reduces precipitation likelihood over Arizona (Fig. 2) and given how Arizona dry periods on monthly (Fig. S2) and 3-monthly time scales (Fig. 3) are associated with higher than typical S-ridge type occurrences.

The increased occurrence of the S-ridge type during the satellite era is broadly consistent with the findings of Swain et al. (2016), who reported a multidecadal increase in frequency of anomalous seasonal-scale ridge patterns conducive to California precipitation deficits. Although a direct comparison between these studies is difficult, due to different domains, methodology, and seasonal definitions, the notion that trends in certain aspects of ridging have recently contributed to drying trends is consistent between studies. The modest magnitude of observed trends in both Swain et al. (2016) and the present study, however, illustrates the difficulty of discerning robust signals given the high degree of interannual variability in this region and the relative shortness of the observational record. With the degree of interannual variability in ridging seen in past decades (Figs. 5 and 6), it is plausible this trend may not be sustained in coming years. In support of this, Lehner et al. (2018) also found the recent drying trend over the Southwest to be related to trends in regional atmospheric circulation over this period. The authors further demonstrated that the drying trend becomes almost negligible after accounting for internal climate variability driving these regional trends in circulation. The seasonality of these observed trends (Fig. S5) is also interesting in light of recent work suggesting that increased greenhouse gas forcing may in the future result in pronounced autumn and spring drying across California and parts of the Colorado River basin (e.g., Ting et al. 2018; Swain et al. 2018).

Targeted model experiments could be used in future research to further untangle if a forced anthropogenic component has contributed to this trend compared to natural internal variability. We suggest that the feature tracking approach in the present analysis could be applied to climate model experiments and used to formally determine whether a forced anthropogenic component has contributed to this trend. Other recent studies

analyzing the CMIP5 and CESM Large Ensemble simulations have reported a trend toward increasing intra-annual and subseasonal precipitation variability in California and adjacent regions under scenarios of increased greenhouse gas forcing (Berg and Hall 2015; Dettinger 2016; Dong et al. 2018), despite only modest changes in average precipitation (Swain et al. 2018). This projected increase in regional precipitation ''volatility'' occurs through a simultaneous increase in both wet and dry extremes, including an especially large increase frequency of years with very low precipitation across Southern California and the interior Southwest (including Arizona). This contrasts with the Pacific Northwest (Washington and Oregon), where the frequency of very low precipitation years is not projected to increase (or is even projected to decrease; Swain et al. 2018). These previous findings are interesting in light of the modest observed trend toward increasing S-ridge frequency (which have historically favored California and Arizona drought; Figs. 2 and 3) but the lack of any corresponding trend in the N-ridge frequency (which favors Oregon and Washington drought; Fig. 5). Collectively, this highlights that the application of geographically nuanced ridging metrics (such as the ridge detection approach outlined in this manuscript) would be valuable for further interpretation of climate model simulations.

The climatology of the tracked ridge types has provided an opportunity to investigate possible remote sources of predictability in greater detail. It is found that different ridge types have rather unique opportunities for predictability (e.g., Fig. 8), such that separating ridge types in this way can better elucidate different remote sources that collectively influence meteorological drought across this region. In particular, it was found that western Pacific tropical SST anomalies, ENSO, and MJO (at lead times extending beyond the weather time scale) are associated with different occurrence likelihoods of ridge types. For ENSO, the largest association is through La Niña (El Niño) increasing (decreasing) the likelihood of the W-ridge and S-ridge types. Notably, certain measures of Pacific tropical SST variability are found to better capture these associations, depending on the ridge type (Fig. 8). For example, the S-ridge-type frequency is more strongly associated with the Niño-3.4 index while the W-ridge and N-ridge types appear to be related to SST variability farther to the west (i.e., through the Niño-4 and SST-WP indices). Irrespective of the particular measure of Pacific tropical SST variability, these associations are typically stronger for the latter half of the water year implying better opportunities for predictability over these months.

These findings are consistent with, but add extra detail to, results from a simple composite analysis of Z500 by ENSO phase (e.g., Garfinkel et al. 2012) and the more general understanding of how ENSO influences precipitation in this region (e.g., Seager et al. 2015). The results from Teng and Branstator (2017) and also Swain et al. (2017) suggest that tropical heating anomalies in regions unrelated to ENSO and MJO may also offer opportunities for extended predictability. However, it is important to emphasize that these associations must be viewed probabilistically, given the known diversity between ENSO events themselves and the diversity in atmospheric circulation responses between similar ENSO events (e.g., Lee et al. 2018). Another consideration is the somewhat limited sample size (here 1950–2014) when examining these teleconnections in observational data alone; given the influence of internal variability, future research may benefit from carrying out a similar methodology with large initial-condition model ensembles (e.g., Deser et al. 2017).

The pattern of SST correlations with the W-ridge type in Fig. 7, while bearing some resemblance to ENSO, also shows meridional structure suggesting some influence by other non-ENSO coupled ocean–atmosphere variability in the Pacific basin. This meridional correlation pattern is also found for the N-ridge type particularly over the January–March months (Fig. S8). Figure 8b shows relatively strong statistically significant ($p < 0.01$) correlations between the PMM and the N-ridge type (positive correlation) and the W-ridge type (negative correlation) over these months, suggesting associations with Pacific SST variability unrelated to ENSO. However, the PMM relationships are stronger for January–March (compared to October–December), over which months the PMM SST structure typically develops in response to forcing by atmospheric circulation variability (Amaya 2019). In contrast, an already mature PMM structure in late boreal autumn might be expected to influence the larger-scale circulation in the Pacific basin (Amaya 2019), relevant to the W-ridge type in the start of the water year, although observational evidence for this was not found to be strong in the present study. A possible reason for this is that the atmospheric circulation response to the PMM near the start of the water year may not project cleanly on to the ridge type locations used in this study, and our results do not rule out the possibility that the PMM may still exert a significant control on atmospheric river conditions across autumn months.

In terms of the MJO and opportunities for extended S2S predictability, a significant increase in the likelihood of particular ridge types is observed at longer lead times. Although other studies have explored links between MJO and ''blocking'' in detail (e.g., Henderson et al. 2016), the ridging results from the present study are more specifically tailored toward precipitation deficits across the region. Certain forecasts of opportunity after strong

MJO events may offer extended prediction skill including after MJO phases 3–6 for the W-ridge type and after MJO phases 4–5 for the N- and S-ridge types. As such, empirical models might potentially offer skillful S2S predictions by capitalizing on these forecasts of opportunity. Indeed, in cases where MJO is skillfully predicted at 2-week lead by dynamical methods, these additional empirical associations could potentially extend S2S probabilistic forecasts into 1-month lead times. As shown in Fig. 9, particularly for the N-ridge-type response, a smoothly varying signal with lead time is evident. For example, the MJO phase-5 response at a lead time of ~5–12 days is similar to the response of MJO phase-4 response at ~13–20 days. This smoothly varying response occurs partly because of the characteristic MJO phase transitions that typically occur every 3–6 days (Wheeler and Hendon 2004; Tseng et al. 2018). Indeed, recent studies have proposed that skillful empirical S2S forecasts (e.g., for temperature and ARs) can be obtained by incorporating this smoothly varying MJO response into forecasts (Baggett et al. 2017; Jenney et al. 2019), with our results suggesting that similar success could be obtained for predicting particular ridge events relevant to precipitation deficits across the western United States.

In terms of a possible high-latitude influence on ridging relevant to drought, the Arctic Oscillation (AO) was found to be positively correlated with both the W-ridge frequency and persistence across all October–March months (Fig. 8 and Fig. S11), although the N- and S-ridge types generally showed no association. This finding is broadly consistent with recent studies showing an important influence of the AO on West Coast precipitation (Singh et al. 2018) and, given that there is some emerging skill in seasonal prediction of the AO (e.g., Riddle et al. 2013; Scaife et al. 2014), improved longer-lead predictions of meteorological drought in certain parts of the Southwest may be possible through the AO to W-ridge-type association pathway shown here.

Concurrent sea ice correlations with ridging characteristics were generally found to be weak; however, the strongest and most notable of these correlations (for the W-ridge type, over particular months and regions; Fig. 8) may approach the typical correlation strength of tropical SSTs. Somewhat stronger (negative) correlations with sea ice were also found when considering ridge magnitude (as opposed to ridge frequency or persistence; Fig. S12). Possible links with sea ice were only briefly examined here from observational data alone, and it was beyond the scope of this study to investigate potential causal mechanisms. Indeed, noncausal correlations could potentially emerge by confounders that jointly influence both sea ice and ridging, such as tropical SSTs (Meehl et al. 2018; Blackport and Screen 2019). The extent to which midlatitude ridging is influenced by high-latitude sea ice variability in winter remains an active area of research (e.g., Swain et al. 2017; Cohen et al. 2018). In targeted model experiments, Blackport and Screen (2019) show a weakening of the eddy-driven jet in response to Arctic sea ice that occurs predominantly in winter, although the impact on ridging was mainly confined to the North Atlantic region. Another suggested mechanism is through sea ice loss (or snow cover changes) enhancing wave activity fluxes into the polar stratosphere to trigger sudden stratospheric warming events. However, this influence is also found to be largest for ridging across the eastern United States (Cohen et al. 2018). It is also plausible that the relationship between sea ice and midlatitude ridging relevant to western/southwestern U.S. drought will become more evident as Arctic sea ice retreats farther in coming decades (e.g., Cvijanovic et al. 2017). However, at present, our results suggest that if sea ice conditions can indeed improve S2S predictability of drought-relevant ridging, such improvements will likely be modest for this particular region.

While we have discussed the added value of feature tracking (e.g., in terms of characterizing a wider diversity of ridging features that collectively influence precipitation deficits and drought) this approach is not without limitations. The approach implemented in this study targeted key regions based on the spatial covariance between ridging and precipitation, as relevant to widespread meteorological drought across extended winter months. However, additional variables such as incoming solar radiation, humidity, and wind speed, which are relevant to other types of drought through evaporative demand, are likely driven by somewhat different large-scale circulation features not explicitly represented in our analysis. In specific regions, highly localized features of the circulation may also not necessarily be represented. For example, offshore Santa Ana winds associated with warm and dry conditions in Southern California (over autumn and winter) are driven by a range of synoptic conditions (e.g., a high–low pressure dipole) and more localized thermodynamic drivers in the boundary layer (e.g., Conil and Hall 2006).

While beyond the scope of this study, future research may benefit from applying the ridge types described here to further improve the dynamical understanding of particularly large or persistent ridging events. Possible future research avenues include investigating how different individual ridge types typically form and develop in relation to nonlinear Rossby wave breaking, as shown to be often important in this region for influencing ARs by Mundhenk et al. (2016) and Hu et al. (2017). While ridging events were shown to modulate the occurrence likelihood and landfall location of AR events, the potential

for ARs themselves to influence ridging persistence downstream was not examined. In particular, future research may investigate whether ridging predictability can be extended by targeting moist processes through enhanced diabatic heating as a mechanism for Rossby wave breaking favoring persistent ridging in this region (e.g., Pfahl et al. 2015; Woollings et al. 2018). Last, localized SST was found to be related to an enhanced N-ridge-type frequency (Fig. 7), although this statistical relationship tends to diminish at longer lead times (Fig. S9), future research may investigate whether this is partly related to a physical mechanism where warm local SSTs support an amplified or more persistent ridge on submonthly time scales (e.g., Swain et al. 2017; Myers et al. 2018). Meanwhile, remote tropical (west Pacific) SST was found to be related to S- and W-type ridges with lead times as long as 2 months, reinforcing previous findings regarding the potential for subseasonal predictability (i.e., Teng and Branstator 2017; Swain et al. 2017).

5. Conclusions

This study has introduced a ridge detection algorithm and identified three dominant ridge types that strongly impact ARs and precipitation deficits across the western/southwestern United States. This ridge detection algorithm can be readily applied to different reanalysis products and weather/climate models. The three different ridge types presented here show strong regionality in terms of how they influence precipitation deficits, display different long-term variability and trends, and have different sources of remote predictability. Separating out different ridge types in this way has provided insight into the possible extension of prediction skill beyond the weather time scale and into the S2S time scale, desirable for water resource management purposes. Future work will evaluate the representation of these ridge types in operational S2S weather models and examine existing limits and barriers to extended S2S forecasting skill.

Acknowledgments. Monthly AO index data were obtained from CPC: https://www.cpc.ncep.noaa.gov/products/precip/CWlink/daily_ao_index/monthly.ao.index.b50.current.ascii. The Nino3.4 index data were obtained from CPC: http://www.cpc.ncep.noaa.gov/data/indices/
The Nino4 index data were obtained from KNMI: https://climexp.knmi.nl/data/iersst_nino4a_rel.dat
The SOI index data were obtained from the BOM: ftp://ftp.bom.gov.au/anon/home/ncc/www/sco/soi/soiplaintext.html
Monthly PMM index data based on Chiang and Vimont (2004) were obtained from: http://www.aos.wisc.edu/~dvimont/MModes/Data.html
The Colorado River Basin shapefile was obtained from the USDA: https://www.nrcs.usda.gov/wps/PA_NRCSConsumption/download?cid=stelprdb1257068&ext=zip
This study received funding from the California Department of Water Resources (JPL/Caltech Task #82-19834) to support authors PBG, DEW, BG, MDF, and FMR. Authors PBG and DEW also received funding from NASA National Climate Assessment support (JPL/Caltech Task #80NM0018F0563). DLS was supported by a joint collaboration between the Institute of the Environment and Sustainability at the University of California, Los Angeles; the Center for Climate and Weather Extremes at the National Center for Atmospheric Research; and the Nature Conservancy of California. PBG and DEW's contribution to this research was carried out at the Jet Propulsion Laboratory, California Institute of Technology, under a contract with NASA.

REFERENCES

Amaya, D. J., 2019: The Pacific Meridional Mode and ENSO: A review. *Curr. Climate Change Rep.*, **5**, 296–307, https://doi.org/10.1007/s40641-019-00142-x.

Baggett, C. F., E. A. Barnes, E. D. Maloney, and B. D. Mundhenk, 2017: Advancing atmospheric river forecasts into subseasonal-to-seasonal time scales. *Geophys. Res. Lett.*, **44**, 7528–7536, https://doi.org/10.1002/2017GL074434.

Berg, N., and A. Hall, 2015: Increased interannual precipitation extremes over California under climate change. *J. Climate*, **28**, 6324–6334, https://doi.org/10.1175/JCLI-D-14-00624.1.

Blackport, R., and J. A. Screen, 2019: Influence of Arctic sea ice loss in autumn compared to that in winter on the atmospheric circulation. *Geophys. Res. Lett.*, **46**, 2213–2221, https://doi.org/10.1029/2018GL081469.

Cayan, D. R., and J. O. Roads, 1984: Local relationships between United States West Coast precipitation and monthly mean circulation parameters. *Mon. Wea. Rev.*, **112**, 1276–1282, https://doi.org/10.1175/1520-0493(1984)112<1276:LRBUSW>2.0.CO;2.

Chen, M., and A. Kumar, 2018: Winter 2015/16 atmospheric and precipitation anomalies over North America: El Niño response and the role of noise. *Mon. Wea. Rev.*, **146**, 909–927, https://doi.org/10.1175/MWR-D-17-0116.1.

Chiang, J. C. H., and D. J. Vimont, 2004: Analogous Pacific and Atlantic meridional modes of tropical atmosphere–ocean variability. *J. Climate*, **17**, 4143–4158, https://doi.org/10.1175/JCLI4953.1.

Cohen, J., K. Pfeiffer, and J. A. Francis, 2018: Warm Arctic episodes linked with increased frequency of extreme winter weather in the United States. *Nat. Commun.*, **9**, 869, https://doi.org/10.1038/s41467-018-02992-9.

Compo, G. P., and Coauthors, 2011: The Twentieth Century Reanalysis Project. *Quart. J. Roy. Meteor. Soc.*, **137**, 1–28, https://doi.org/10.1002/qj.776.

Conil, S., and A. Hall, 2006: Local regimes of atmospheric variability: A case study of Southern California. *J. Climate*, **19**, 4308–4325, https://doi.org/10.1175/JCLI3837.1.

Cook, B. I., A. P. Williams, J. S. Mankin, R. Seager, J. E. Smerdon, and D. Singh, 2018: Revisiting the leading drivers of Pacific

coastal drought variability in the contiguous United States. *J. Climate*, **31**, 25–43, https://doi.org/10.1175/JCLI-D-17-0172.1.

Cvijanovic, I., B. D. Santer, C. Bonfils, D. D. Lucas, J. C. H. Chiang, and S. Zimmerman, 2017: Future loss of Arctic sea-ice cover could drive a substantial decrease in California's rainfall. *Nat. Commun.*, **8**, 1947, https://doi.org/10.1038/s41467-017-01907-4.

Davini, P., C. Cagnazzo, S. Gualdi, and A. Navarra, 2012: Bidimensional diagnostics, variability, and trends of Northern Hemisphere blocking. *J. Climate*, **25**, 6496–6509, https://doi.org/10.1175/JCLI-D-12-00032.1.

Dee, D. P., and Coauthors, 2011: The ERA-Interim reanalysis: Configuration and performance of the data assimilation system. *Quart. J. Roy. Meteor. Soc.*, **137**, 553–597, https://doi.org/10.1002/qj.828.

DeFlorio, M. J., D. E. Waliser, B. Guan, D. A. Lavers, F. M. Ralph, and F. Vitart, 2018: Global assessment of atmospheric river prediction skill. *J. Hydrometeor.*, **19**, 409–426, https://doi.org/10.1175/JHM-D-17-0135.1.

——, ——, ——, F. M. Ralph, and F. Vitart, 2019: Global evaluation of atmospheric river subseasonal prediction skill. *Climate Dyn.*, **52**, 3039–3060, https://doi.org/10.1007/s00382-018-4309-x.

Deser, C., I. R. Simpson, K. A. McKinnon, and A. S. Phillips, 2017: The Northern Hemisphere extratropical atmospheric circulation response to ENSO: How well do we know it and how do we evaluate models accordingly? *J. Climate*, **30**, 5059–5082, https://doi.org/10.1175/JCLI-D-16-0844.1.

Dettinger, M. D., 2013: Atmospheric rivers as drought busters on the U.S. West Coast. *J. Hydrometeor.*, **14**, 1721–1732, https://doi.org/10.1175/JHM-D-13-02.1.

——, 2016: Historical and future relations between large storms and droughts in California. *San Francisco Estuary Watershed Sci.*, **14**, 1–21, https://doi.org/10.15447/sfews.2016v14iss2art1.

——, F. M. Ralph, T. Das, P. J. Neiman, and D. R. Cayan, 2011: Atmospheric rivers, floods and the water resources of California. *Water*, **3**, 445–478, https://doi.org/10.3390/w3020445.

Dole, R. M., 1986: Persistent anomalies of the extratropical Northern Hemisphere wintertime circulation: Structure. *Mon. Wea. Rev.*, **114**, 178–207, https://doi.org/10.1175/1520-0493(1986)114<0178:PAOTEN>2.0.CO;2.

Dong, L., L. R. Leung, and F. Song, 2018: Future changes of subseasonal precipitation variability in North America during winter under global warming. *Geophys. Res. Lett.*, **45**, 12 467–12 476, https://doi.org/10.1029/2018GL079900.

Garfinkel, C. I., A. H. Butler, D. W. Waugh, M. M. Hurwitz, and L. M. Polvani, 2012: Why might stratospheric sudden warmings occur with similar frequency in El Niño and La Niña winters? *J. Geophys. Res.*, **117**, D19106, https://doi.org/10.1029/2012JD017777.

Gelaro, R., and Coauthors, 2017: The Modern-Era Retrospective Analysis for Research and Applications, version 2 (MERRA-2). *J. Climate*, **30**, 5419–5454, https://doi.org/10.1175/JCLI-D-16-0758.1.

Gibson, P. B., S. E. Perkins-Kirkpatrick, P. Uotila, A. S. Pepler, and L. V. Alexander, 2017: On the use of self-organizing maps for studying climate extremes. *J. Geophys. Res. Atmos.*, **122**, 3891–3903, https://doi.org/10.1002/2016JD026256.

——, D. E. Waliser, H. Lee, B. Tian, and E. Massoud, 2019: Climate model evaluation in the presence of observational uncertainty: Precipitation indices over the contiguous United States. *J. Hydrometeor.*, **20**, 1339–1357, https://doi.org/10.1175/JHM-D-18-0230.1.

Guan, B., and D. E. Waliser, 2015: Detection of atmospheric rivers: Evaluation and application of an algorithm for global studies. *J. Geophys. Res. Atmos.*, **120**, 12 514–12 535, https://doi.org/10.1002/2015JD024257.

——, ——, N. P. Molotch, E. J. Fetzer, and P. J. Neiman, 2012: Does the Madden–Julian Oscillation influence wintertime atmospheric rivers and snowpack in the Sierra Nevada? *Mon. Wea. Rev.*, **140**, 325–342, https://doi.org/10.1175/MWR-D-11-00087.1.

——, N. P. Molotch, D. E. Waliser, E. J. Fetzer, and P. J. Neiman, 2013: The 2010/2011 snow season in California's Sierra Nevada: Role of atmospheric rivers and modes of large-scale variability. *Water Resour. Res.*, **49**, 6731–6743, https://doi.org/10.1002/wrcr.20537.

Guirguis, K., A. Gershunov, R. E. S. Clemesha, T. Shulgina, A. C. Subramanian, and F. M. Ralph, 2018: Circulation drivers of atmospheric rivers at the North American west coast. *Geophys. Res. Lett.*, **45**, 12 576–12 584, https://doi.org/10.1029/2018GL079249.

——, ——, T. Shulgina, R. E. S. Clemesha, and F. M. Ralph, 2019: Atmospheric rivers impacting Northern California and their modulation by a variable climate. *Climate Dyn.*, **52**, 6569–6583, https://doi.org/10.1007/S00382-018-4532-5.

Hayes, M. J., M. D. Svoboda, D. A. Wilhite, and O. V. Vanyarkho, 1999: Monitoring the 1996 drought using the standardized precipitation index. *Bull. Amer. Meteor. Soc.*, **80**, 429–438, https://doi.org/10.1175/1520-0477(1999)080<0429:MTDUTS>2.0.CO;2.

Henderson, S. A., E. D. Maloney, and E. A. Barnes, 2016: The influence of the Madden–Julian oscillation on Northern Hemisphere winter blocking. *J. Climate*, **29**, 4597–4616, https://doi.org/10.1175/JCLI-D-15-0502.1.

Hendon, H. H., 1986: Streamfunction and velocity potential representation of equatorially trapped waves. *J. Atmos. Sci.*, **43**, 3038–3042, https://doi.org/10.1175/1520-0469(1986)043<3038:SAVPRO>2.0.CO;2.

Hirahara, S., M. Ishii, and Y. Fukuda, 2014: Centennial-scale sea surface temperature analysis and its uncertainty. *J. Climate*, **27**, 57–75, https://doi.org/10.1175/JCLI-D-12-00837.1.

Horton, D. E., N. C. Johnson, D. Singh, D. L. Swain, B. Rajaratnam, and N. S. Diffenbaugh, 2015: Contribution of changes in atmospheric circulation patterns to extreme temperature trends. *Nature*, **522**, 465–469, https://doi.org/10.1038/nature14550.

Hoskins, B., and K. Hodges, 2019: The annual cycle of Northern Hemisphere storm tracks. Part I: Seasons. *J. Climate*, **32**, 1743–1760, https://doi.org/10.1175/JCLI-D-17-0870.1.

Hu, H., F. Dominguez, Z. Wang, D. A. Lavers, G. Zhang, and F. M. Ralph, 2017: Linking atmospheric river hydrological impacts on the U.S. West Coast to Rossby wave breaking. *J. Climate*, **30**, 3381–3399, https://doi.org/10.1175/JCLI-D-16-0386.1.

Huang, B., and Coauthors, 2017: Extended Reconstructed Sea Surface Temperature, version 5 (ERSSTv5): Upgrades, validations, and intercomparisons. *J. Climate*, **30**, 8179–8205, https://doi.org/10.1175/JCLI-D-16-0836.1.

Jenney, A. M., K. M. Nardi, E. A. Barnes, and D. A. Randall, 2019: The seasonality and regionality of MJO impacts on North American temperature. *Geophys. Res. Lett.*, **46**, 9193–9202, https://doi.org/10.1029/2019GL083950.

Jong, B.-T., M. Ting, R. Seager, N. Henderson, and D. E. Lee, 2018: Role of equatorial Pacific SST forecast error in the late winter California precipitation forecast for the 2015/16 El Niño. *J. Climate*, **31**, 839–852, https://doi.org/10.1175/JCLI-D-17-0145.1.

Kulkarni, A., and H. von Storch, 1995: Monte Carlo experiments on the effect of serial correlation on the Mann-Kendall test of trend. *Meteor. Z.*, **4**, 82–85, https://doi.org/10.1127/metz/4/1992/82.

Lee, S. K., H. Lopez, E. S. Chung, P. DiNezio, S. W. Yeh, and A. T. Wittenberg, 2018: On the fragile relationship between El Niño and California rainfall. *Geophys. Res. Lett.*, **45**, 907–915, https://doi.org/10.1002/2017GL076197.

Lehner, F., C. Deser, I. R. Simpson, and L. Terray, 2018: Attributing the U.S. Southwest's recent shift into drier conditions. *Geophys. Res. Lett.*, **45**, 6251–6261, https://doi.org/10.1029/2018GL078312.

Liu, P., and Coauthors, 2018: Climatology of tracked persistent maxima of 500-hPa geopotential height. *Climate Dyn.*, **51**, 701–717, https://doi.org/10.1007/s00382-017-3950-0.

Masato, G., B. J. Hoskins, and T. Woollings, 2013: Wave-breaking characteristics of Northern Hemisphere winter blocking: A two-dimensional approach. *J. Climate*, **26**, 4535–4549, https://doi.org/10.1175/JCLI-D-12-00240.1.

Meehl, G. A., C. T. Y. Chung, J. M. Arblaster, M. M. Holland, and C. M. Bitz, 2018: Tropical decadal variability and the rate of Arctic sea ice decrease. *Geophys. Res. Lett.*, **45**, 11 326–11 333, https://doi.org/10.1029/2018GL079989.

Morss, R. E., J. K. Lazo, B. G. Brown, H. E. Brooks, P. T. Ganderton, and B. N. Mills, 2008: Societal and economic research and applications for weather forecasts: Priorities for the North American THORPEX program. *Bull. Amer. Meteor. Soc.*, **89**, 335–346, https://doi.org/10.1175/BAMS-89-3-335.

Mundhenk, B. D., E. A. Barnes, E. D. Maloney, and K. M. Nardi, 2016: Modulation of atmospheric rivers near Alaska and the U.S. West Coast by Northeast Pacific height anomalies. *J. Geophys. Res. Atmos.*, **121**, 12 751–12 765, https://doi.org/10.1002/2016jd025350.

——, ——, ——, and C. F. Baggett, 2018: Skillful empirical subseasonal prediction of landfalling atmospheric river activity using the Madden–Julian Oscillation and quasi-biennial oscillation. *npj Climate Atmos. Sci.*, **1**, 20177, https://doi.org/10.1038/S41612-017-0008-2.

Myers, T. A., C. R. Mechoso, G. V. Cesana, M. J. DeFlorio, and D. E. Waliser, 2018: Cloud feedback key to marine heatwave off Baja California. *Geophys. Res. Lett.*, **45**, 4345–4352, https://doi.org/10.1029/2018GL078242.

Newman, M., and P. D. Sardeshmukh, 1998: The impact of the annual cycle on the North Pacific/North American response to remote low-frequency forcing. *J. Atmos. Sci.*, **55**, 1336–1353, https://doi.org/10.1175/1520-0469(1998)055<1336:TIOTAC>2.0.CO;2.

Pandey, G. R., D. R. Cayan, and K. P. Georgakakos, 1999: Precipitation structure in the Sierra Nevada of California during winter. *J. Geophys. Res.*, **104**, 12 019–12 030, https://doi.org/10.1029/1999JD900103.

Parsons, S., J. A. Renwick, and A. J. McDonald, 2016: An assessment of future Southern Hemisphere blocking using CMIP5 projections from four GCMs. *J. Climate*, **29**, 7599–7611, https://doi.org/10.1175/JCLI-D-15-0754.1.

Peng, P., A. Kumar, M. Chen, Z.-Z. Hu, and B. Jha, 2019: Was the North American extreme climate in winter 2013/14 a SST forced response? *Climate Dyn.*, **52**, 3099–3110, https://doi.org/10.1007/S00382-018-4314-0.

Pfahl, S., C. Schwierz, M. Croci-Maspoli, C. M. Grams, and H. Wernli, 2015: Importance of latent heat release in ascending air streams for atmospheric blocking. *Nat. Geosci.*, **8**, 610–614, https://doi.org/10.1038/ngeo2487.

Rayner, S., D. Lach, and H. Ingram, 2005: Weather forecasts are for wimps: Why water resource managers do not use climate forecasts. *Climatic Change*, **69**, 197–227, https://doi.org/10.1007/s10584-005-3148-z.

Reichle, R. H., Q. Liu, R. D. Koster, C. S. Draper, S. P. P. Mahanama, and G. S. Partyka, 2017: Land surface precipitation in MERRA-2. *J. Climate*, **30**, 1643–1664, https://doi.org/10.1175/JCLI-D-16-0570.1.

Renwick, J. A., 2005: Persistent positive anomalies in the Southern Hemisphere circulation. *Mon. Wea. Rev.*, **133**, 977–988, https://doi.org/10.1175/MWR2900.1.

Riddle, E. E., A. H. Butler, J. C. Furtado, J. L. Cohen, and A. Kumar, 2013: CFSv2 ensemble prediction of the wintertime Arctic Oscillation. *Climate Dyn.*, **41**, 1099–1116, https://doi.org/10.1007/s00382-013-1850-5.

Scaife, A. A., and Coauthors, 2014: Skillful long-range prediction of European and North American winters. *Geophys. Res. Lett.*, **41**, 2514–2519, https://doi.org/10.1002/2014GL059637.

Seager, R., and N. Henderson, 2016: On the role of tropical ocean forcing of the persistent North American West Coast ridge of winter 2013/14. *J. Climate*, **29**, 8027–8049, https://doi.org/10.1175/JCLI-D-16-0145.1.

——, N. Harnik, W. A. Robinson, Y. Kushnir, M. Ting, H.-P. Huang, and J. Velez, 2005: Mechanisms of ENSO-forcing of hemispherically symmetric precipitation variability. *Quart. J. Roy. Meteor. Soc.*, **131**, 1501–1527, https://doi.org/10.1256/qj.04.96.

——, and Coauthors, 2015: Causes of the 2011–14 California drought. *J. Climate*, **28**, 6997–7024, https://doi.org/10.1175/JCLI-D-14-00860.1.

Singh, D., M. Ting, A. A. Scaife, and N. Martin, 2018: California winter precipitation predictability: Insights from the anomalous 2015–2016 and 2016–2017 seasons. *Geophys. Res. Lett.*, **45**, 9972–9980, https://doi.org/10.1029/2018GL078844.

Swain, D. L., 2015: A tale of two California droughts: Lessons amidst record warmth and dryness in a region of complex physical and human geography. *Geophys. Res. Lett.*, **42**, 9999–10 003, https://doi.org/10.1002/2015GL066628.

——, M. Tsiang, M. Haugen, D. Singh, A. Charland, B. Rajaratnam, and N. S. Diffenbaugh, 2014: The extraordinary California drought of 2013/2014: Character, context, and the role of climate change [in "Explaining Extremes of 2013 from a Climate Perspective"]. *Bull. Amer. Meteor. Soc.*, **95** (9), S3–S7, https://doi.org/10.1175/1520-0477-95.9.S1.1.

——, D. E. Horton, D. Singh, and N. S. Diffenbaugh, 2016: Trends in atmospheric patterns conducive to seasonal precipitation and temperature extremes in California. *Sci. Adv.*, **2**, e1501344, https://doi.org/10.1126/sciadv.1501344.

——, D. Singh, D. E. Horton, J. S. Mankin, T. C. Ballard, and N. S. Diffenbaugh, 2017: Remote linkages to anomalous winter atmospheric ridging over the northeastern Pacific. *J. Geophys. Res. Atmos.*, **122**, 12 194–12 209, https://doi.org/10.1002/2017JD026575.

——, B. Langenbrunner, J. D. Neelin, and A. Hall, 2018: Increasing precipitation volatility in twenty-first-century California. *Nat. Climate Change*, **8**, 427–433, https://doi.org/10.1038/s41558-018-0140-y.

Takaya, K., and H. Nakamura, 2001: A formulation of a phase-independent wave-activity flux for stationary and migratory quasigeostrophic eddies on a zonally varying basic flow. *J. Atmos. Sci.*, **58**, 608–627, https://doi.org/10.1175/1520-0469(2001)058<0608:AFOAPI>2.0.CO;2.

Teng, H., and G. Branstator, 2017: Causes of extreme ridges that induce California droughts. *J. Climate*, **30**, 1477–1492, https://doi.org/10.1175/JCLI-D-16-0524.1.

Thompson, D. W. J., and J. M. Wallace, 1998: The Arctic oscillation signature in the wintertime geopotential height and temperature fields. *Geophys. Res. Lett.*, **25**, 1297–1300, https://doi.org/10.1029/98GL00950.

Thornton, P. E., M. M. Thornton, B. W. Mayer, Y. Wei, R. Devarakonda, R. S. Vose, and R. B. Cook, 2016: Daymet: daily surface weather data on a 1-km grid for North America, version 3. Oak Ridge National Laboratory Distributed Active Archive Center, accessed 5 April 2019, https://doi.org/10.3334/ORNLDAAC/1328.

Ting, M., R. Seager, C. Li, H. Liu, and N. Henderson, 2018: Mechanism of future spring drying in the Southwestern United States in CMIP5 models. *J. Climate*, **31**, 4265–4279, https://doi.org/10.1175/JCLI-D-17-0574.1.

Titchner, H. A., and N. A. Rayner, 2014: The Met Office Hadley Centre sea ice and sea surface temperature data set, version 2: 1. Sea ice concentrations. *J. Geophys. Res. Atmos.*, **119**, 2864–2889, https://doi.org/10.1002/2013JD020316.

Tseng, K.-C., E. A. Barnes, and E. D. Maloney, 2018: Prediction of the midlatitude response to strong Madden–Julian Oscillation events on S2S time scales. *Geophys. Res. Lett.*, **45**, 463–470, https://doi.org/10.1002/2017GL075734.

Vitart, F., and Coauthors, 2017: The Subseasonal to Seasonal (S2S) prediction project database. *Bull. Amer. Meteor. Soc.*, **98**, 163–173, https://doi.org/10.1175/BAMS-D-16-0017.1.

Vose, R., and Coauthors, 2014: Gridded 5km GHCN-daily temperature and precipitation dataset (nCLIMGRID), version 1.0. NOAA National Centers for Environmental Information, accessed 16 January 2019, https://doi.org/10.7289/V5SX6B56.

Wheeler, M. C., and H. H. Hendon, 2004: An all-season real-time multivariate MJO index: Development of an index for monitoring and prediction. *Mon. Wea. Rev.*, **132**, 1917–1932, https://doi.org/10.1175/1520-0493(2004)132<1917:AARMMI>2.0.CO;2.

Wilks, D. S., 2016: "The stippling shows statistically significant grid points": How research results are routinely overstated and overinterpreted, and what to do about it. *Bull. Amer. Meteor. Soc.*, **97**, 2263–2273, https://doi.org/10.1175/BAMS-D-15-00267.1.

Woollings, T., B. Hoskins, M. Blackburn, and P. Berrisford, 2008: A new Rossby wave–breaking interpretation of the North Atlantic Oscillation. *J. Atmos. Sci.*, **65**, 609–626, https://doi.org/10.1175/2007JAS2347.1.

——, and Coauthors, 2018: Blocking and its response to climate change. *Curr. Climate Change Rep.*, **4**, 287–300, https://doi.org/10.1007/s40641-018-0108-z.

Yue, S., P. Pilon, B. Phinney, and G. Cavadias, 2002: The influence of autocorrelation on the ability to detect trend in hydrological series. *Hydrol. Processes*, **16**, 1807–1829, https://doi.org/10.1002/hyp.1095.

Zhou, Y., and H.-M. Kim, 2018: Prediction of atmospheric rivers over the North Pacific and its connection to ENSO in the North American Multi-Model Ensemble (NMME). *Climate Dyn.*, 1623–1637, https://doi.org/10.1007/S00382-017-3973-6.